Spectral Super Resolution of Hyperspectral Images via Coupled Dictionary Learning

Konstantina Fotiadou, Grigorios Tsagkatakis, and Panagiotis Tsakalides

***Abstract*— High-spectral resolution imaging systems play a critical role in the identification and characterization of objects in a scene of interest. Unfortunately, multiple factors impair spectral resolution, as in the case of modern snapshot spectral imagers that associate each hyperpixel with a specific spectral band. In this paper, we introduce a novel postacquisition computational technique aiming to enhance the spectral dimensionality of imaging systems by exploiting the mathematical frameworks of sparse representations and dictionary learning. We propose a coupled dictionary learning model which considers joint feature spaces, composed of low- and high-spectral resolution hypercubes, in order to achieve spectral superresolution performance. We formulate our spectral coupled dictionary learning optimization problem within the context of the alternating direction method of multipliers, and we manage to update the involved quantities via closed-form expressions. In addition, we consider a realistic spectral subsampling scenario, taking into account the spectral response functions of different satellites. Moreover, we apply our spectral superresolution algorithm on real satellite data acquired by Landsat-8 and Sentinel-2 sensors. Finally, we have investigated the problem of hyperspectral image unmixing using the recovered high-spectral resolution data cube, and we are able to demonstrate that the proposed scheme provides significant value in hyperspectral image understanding techniques. Experimental results demonstrate the ability of the proposed approach to synthesize high-spectral-resolution 3-D hypercubes, achieving better performance compared to state-of-the-art resolution enhancement methods.**

***Index Terms*— Alternating direction method of multipliers, coupled dictionary learning, hyperspectral image enhancement, remote sensing image processing, sparse representations, spectral resolution enhancement, spectral super-resolution.**

I. INTRODUCTION

HIGH RESOLUTION remote-sensing architectures including hyperspectral imagers (HSIs) [1] offer valuable insights regarding the composition of a scene and singicifantly facilitate tasks such as object and material recognition [2], spectral unmixing [3]–[5], and region clustering [6]–[10], among others. To accomplish this goal, hyperspectral imaging systems must capture massive amounts of measurements, encoding the dynamics of the spatial and spectral variations in a scene. Currently deployed Earth observation (EO) satellite platforms provide high-frequency global coverage at a much finer spatial resolution compared to the past. Nevertheless, to achieve this goal, typically a small number of spectral observations is considered (ranging from 3 to 12 spectral bands). The work presented in this paper seeks to address this limitation by demonstrating the ability to increase spectral resolution, and thus the ability to perform spectral characterization of remote sensing imagery.

Achieving high spatial, spectral, and temporal resolution is extremely challenging, due to several architectural constraints and conflicting objectives. A characteristic example of this limitation pertains to the remote sensing community, where multispectral instruments such as QuickBird [11] or IKONOS [12] provide low-spectral (i.e., red green blue (RGB), panchromatic, and near-IR) and high spatial resolution imagery, while other instruments, such as the Hyperion [13] sensor, provide 3-D datacubes with high spectral and low spatial resolution. With regards to the temporal resolution of various satellites, the MODIS [14] multispectral sensor provides global coverage of the entire Earth with a revisit frequency of every one or two days. In contrast, EO-1's Hyperion sensor, has a low temporal resolution, since it is designed to collect hyperspectral data according to tasking requests. Hence, the combination of different sources of information on the various instruments is vital for EO applications. However, instead of using extra hardware components on the satellite instruments to enhance the spatio–spectral or temporal resolution, remote sensing imaging systems require the development of postacquisition enhancement techniques, exploiting the already existing information captured by various satellites. Consider as an example, the scenario where already acquired imagery from different resolution satellites, could be enhanced using training images of the same region, acquired by higher resolution spectrometers aboard newer platforms.

In addition, another severe limitation concerns the commissioning phase of the various instruments. For instance, sensors such as QuickBird or IKONOS have been decommissioned. As a result, these sensors provide only historical data. At this point, another limitation arises from instruments that were malfunctioning, such as the Soil Moisture Active and Passive (SMAP) [15] satellite, which was launched in order to map global soil moisture. SMAP satellite carried two instruments, the radar (active) and the radiometer (passive). Unfortunately, after a short time period, the radar instrument has halted its transmissions. Consequently, the design of a generic algorithmic scheme that could exploit the histori-

---

Manuscript received April 23, 2018; revised September 15, 2018; accepted September 30, 2018. Date of publication November 14, 2018; date of current version April 22, 2019. This work was partially funded by the DEDALE project, contract no. 665044, within the H2020 Framework Program of the European Commission. *(Corresponding author: Konstantina Fotiadou.)*

K. Fotiadou and P. Tsakalides are with the Department of Computer Science, University of Crete, Heraklion 700 13, Greece, and also with the Institute of Computer Science, Foundation for Research & Technology–Hellas, Heraklion 711 10, Greece (e-mail: kfot@ics.forth.gr; tsakalid@ics.forth.gr).

G. Tsagkatakis is with the Institute of Computer Science, Foundation for Research & Technology–Hellas, Heraklion 711 10, Greece (e-mail: greg@ics.forth.gr).

Color versions of one or more of the figures in this paper are available online at http://ieeexplore.ieee.org.

Digital Object Identifier 10.1109/TGRS.2018.2877124

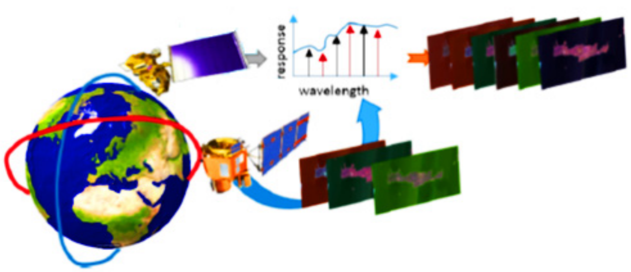

Fig. 1. Case of spectral super resolution in EO. A model built on high–low resolution pairs from two instruments is introduced for increasing spectral resolution.

cal information from the period that both instruments were commissioned or normally operating is crucial to the remote sensing community.

Finally, the demand of capturing simultaneously high spectral and spatial information has led to the design of spectrally resolvable detector array (SRDA) architectures [16], a new generation of *snapshot* spectral imagers, which seek to acquire the entire 3-D hypercube over a single integration period. By employing advanced detector fabrication processes, SRDA architectures associate each pixel with a single spectral band according to a pattern that is repeated over the spatial dimensions of the detector. Despite the dramatic improvement these architectures offer with respect to acquisition time, they also lead to a reduction of the spatio–spectral resolution since only a single spectral band is captured by each spatial detector element [17], [18]. As a result, it is of great importance the design of a postacquisition technique, able to overcome the tradeoff between the spatial, spectral, and temporal resolutions.

In this paper, we propose a novel computational imaging technique that addresses the concept of *spectral superresolution*, where low and high spectral resolution training examples are used within a machine learning framework to increase the spectral resolution of existing imaging systems. The main motivation in the spectral superresolution problem is the inability of existing remote sensing imaging sensors to provide simultaneously high spatial and spectral imaging 3-D data cubes. Consequently, our algorithm can be relevant in a wide range of remote sensing applications for EO.

For instance, acquired imagery from low spectral resolution satellites, e.g., MODIS [14] or Sentinel-2 [19], could be enhanced using images acquired over the same region from higher resolution spectrometers, such as the EO-1 Hyperion sensor [13], as illustrated in Fig. 1. Moreover, our algorithm can be valuable in enhancing the spectral dimension of existing historical remote sensing data acquired in the past from satellites that have been decommissioned. In addition, our scheme could be considered for relaxing data communication requirements by training with high-resolution data during the commission phase and by reducing the required bandwidth during normal operation.

The proposed *spectral coupled dictionary learning* (SCDL) algorithm capitalizes on the *sparse representations* (SRs) framework [20] and extents it by introducing a *coupled dictionary learning* process. Furthermore, we solve the SCDL problem within the highly efficient alternating direction method of multipliers (ADMMs) optimization framework [21], [22]. The key contributions of this paper can be summarized as follows.

1) The formulation of a novel, postacquisition approach for the enhancement of low spectral resolution multispectral and hyperspectral imagery.
2) The design of an efficient coupled dictionary learning architecture, relying on the ADMMs.
3) The investigation of a realistic spectral downsampling scenario, using the spectral signatures of different satellites.
4) The systematic evaluation of the proposed spectral resolution enhancement approach on real remote sensing multispectral and hyperspectral data sets.

A key benefit of the proposed method is its flexibility since it can be considered for the enhancement of various pairs of low- and high-resolution imagery.

The remainder of this paper is organized as follows. Section II provides an overview of the related state of the art. Section III presents the proposed spectral superresolution scheme of multispectral and hyperspectral imagery, whereas Section IV develops the coupled spectral dictionary learning methodology. Section V provides the data sources and the spectral downsampling processes, along with the experimental results on both synthetic and real earth observation data. In addition, in Section V, we demonstrate the impact of the proposed SCDL technique on the hyperspectral image unmixing problem. Extensions of this paper are discussed in Section VI.

II. RELATED WORK

In this section, we overview several representative approaches that address the problem of spatial and spectral resolution enhancement of hyperspectral imagery, as well as the techniques for learning coupled feature spaces. Although enhancing the spatial, spectral, and temporal resolution of HSI imagery is a subject of significant research, most of the efforts have focused on improving spatial resolution [23]. Unfortunately, only a few techniques have been proposed in the literature, which solve the problem of spectral super resolution. In the following paragraphs, we provide in great detail the most representative multispectral and hyperspectral image enhancement techniques.

State-of-the-art spatial resolution enhancement approaches may be classified into two representative categories, namely, pan sharpening [24], [25], [25]–[30] and spatio–spectral fusion [31]–[37]. On the one hand, pan sharpening combines low spatial resolution multispectral and hyperspectral scenes, along with corresponding high spatial resolution panchromatic images, to synthesize spatially superresolved 3-D data cubes. This is achieved either by replacing the component containing the spatial structure from the HSI image with the panchromatic image [38], or by decomposing the panchromatic image and by resampling it to multispectral bands [39]. In both cases, pan-sharpening methods rely on a particular architecture where a high spatial resolution panchromatic camera shares the same field of view with a limited resolution spectral imaging system. In addition, Guo *et al.* [40] tackled the image pan-sharpening problem by utilizing an online coupled dictionary learning technique, where a low spatial resolution multispectral image is fused with a high spatial resolution panchromatic image to obtain a high spatial resolution multispectral image. More recent spatial superresolution approaches based on learning and neural networks are reported in [41]–[43]. Contrary to the aforementioned techniques, in this paper, we propose a novel scheme that efficiently learns *coupled* feature spaces, overcoming the limitations arising from independent dictionary learning.

On the other hand, spatio–spectral fusion approaches improve spatial resolution by exploiting the relation between the spatial and the spectral variations of HSI scenes. Yokoya *et al.* [33] present a comparative review of several multispectral and hyperspectral fusion techniques. Bieniarz *et al.* [44] describe how to enhance the spatial dimension of HSI by employing a sparse spectral unmixing technique and by fusing the results with the multispectral imagery. Similarly, a joint superresolution and unmixing approach are proposed in [45], based on an SR in the spatial domain and a spectral unmixing in the spectral domain. Erturk *et al.* [47] develop in a spatial superresolution technique utilizing a fully constrained least squares spectral unmixing scheme with a spatial regularization based on modified binary particle swarm optimization. Dong *et al.* [47] propose a nonnegative sparsity-based hyperspectral superresolution technique, combining a low-resolution hyperspectral image with a high-resolution RGB image and employing a single dictionary learning scheme to model the relations between the low spectral resolution HSI and the corresponding high-resolution RGB images. Akhtar *et al.* [48] propose a Bayesian sparse coding method, utilizing Bayesian nonparametric dictionary learning to enhance the spatial variation of multispectral and hyperspectral imagery. Finally, Yin *et al.* [50] combine interpolated low-resolution images with fused images in order to learn their internal SR and to reconstruct the high-resolution version of the scene. Before learning the SR, the authors extract the low- and high-frequency components of the interpolated low-resolution scenes.

An important class of image enhancement techniques considers transferring information between different feature spaces. For instance, Yang *et al.* [50] address the traditional RGB image superresolution problem by constructing joint dictionaries for the low- and high-resolution spaces under the assumption that the two representations share the same sparse coding. As an extension, in [51], a coupled dictionary learning scheme based on bilevel optimization is proposed and applied to the problems of single-image superresolution and compressed sensing recovery. Although the specific bilevel dictionary learning approach achieves low reconstruction error, the same, possibly suboptimal, sparse coding is still utilized among the different feature spaces. Consequently, accurate recovery is not assured by the jointly learned dictionaries. In addition, He *et al.* [52] proposes a beta process-based coupled dictionary learning approach by obtaining SRs with the same sparsity measure, but with different values in the coupled feature spaces. In contrast, Fotiadou *et al.* [53] tackle the problem of spectroscopic data denoising, by exploiting a novel coupled dictionary learning scheme based on the ADMMs [21].

As opposed to spatial superresolution, enhancing the *spectral* dimension of HSI scenes has drawn little attention. Charles *et al.* [55] introduced a sparsity-based spectral superresolution approach for hyperspectral images by learning a dictionary of spectral signatures that decomposes the spectral response of each hyperpixel. Specifically, they enhance the spectral dimension of multispectral to hyperspectral level by learning an approximation to the data manifold. As an extension of this paper, the authors introduced in [55] a reweighted ℓ_1 spatial filtering technique that improves with greater accuracy the spectral superresolution of remote sensing imagery. In this paper, we enhance directly the spectral dimension of remote sensing imagery without impairing the spatial superresolution. As a result, no further spatial filtering is needed for improving the spatial resolution.

Charles *et al.* [57] consider geographically colocated multispectral and hyperspectral oceanic water-color images and they enhance the limited multispectral measurements utilizing a sparse-based approach. First, they use a spectral-mixing formulation and they define the measured spectrum for each pixel as the sum of the weighted material spectra. The desired high-resolution spectra are expressed as the linear combination between a blurring matrix and the measured spectra. As a result, the authors take into consideration a blurring operator that represents how the measured (input) spectra are related to the desired (target) hyperspectral spectra. This blurring operator can be considered as an operator that either merges neighboring spectral bands together (i.e., a blurring operator) or omits completely the spectral bands. Consequently, the authors interpret the spectral superresolution problem as a traditional image denoising problem, which is efficiently solved via a sparse decomposition technique. Our proposed coupled dictionary learning scheme directly learns the coupled feature spaces without requiring the knowledge of a blurring kernel. As a result, our approach can be applied in any type of remote sensing or terrestrial scenario that requires the enhancement of the spectral dimension.

Recently, we proposed several techniques exploiting the low-rank matrix completion framework for superresolving low spatial resolution HSI scenes. In [17], we construct a high spatial and spectral resolution hypercube from undersampled snapshot mosaic imagery. In [57], we employ an alternating minimization coupled dictionary learning technique that is applicable to arbitrary low–high resolution pairs. The work in this paper is an extension of an earlier sparsity-based approach [58] employing independent dictionaries that model the low and high spectral resolution feature spaces. To the best of our knowledge, this is the first work that applies a *coupled* sparse dictionary learning architecture to the problem of spectral resolution enhancement of HSI data.

III. SPECTRAL RESOLUTION ENHANCEMENT

The proposed approach synthesizes a high-spectral resolution hypercube from its low spectral resolution acquired version by capitalizing on the *SRs* learning framework [20]. According to the SR framework, examples extracted from

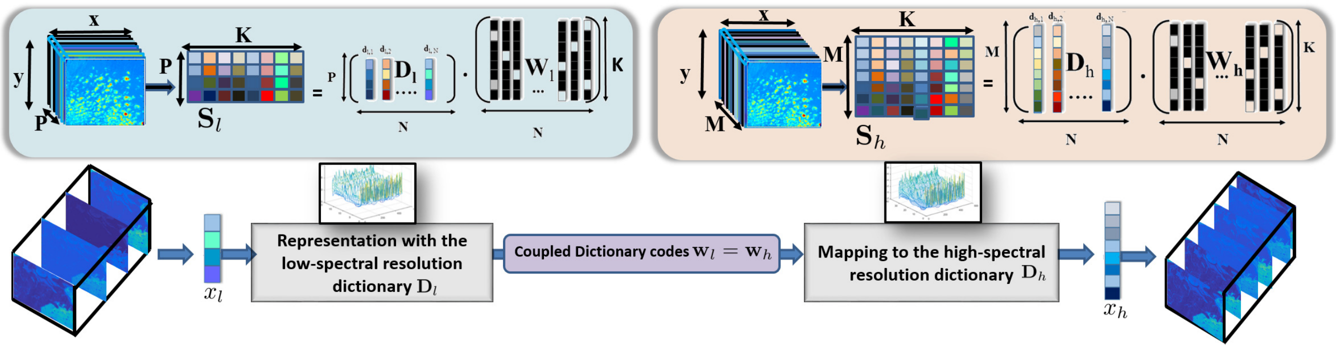

Fig. 2. SCDL System Block Diagram. System takes as input a hypercube acquired with a limited number of spectral bands and produces an estimate of an extended spatio–spectral hypercube. During training, multiple high- and low-spectral resolution hyperpixels are extracted from training hypercubes. Given these hyperpixel pairs, a coupled dictionary learning scheme is employed for learning two sparsifying dictionaries, corresponding to the two resolution cases. During runtime, low-resolution hyperpixels are mapped to the low-resolution dictionary and the identified sparse coding coefficients are combined with the high-resolution dictionary for producing the final estimates.

hyperspectral images can be represented as sparse linear combinations of elements from learned overcomplete dictionaries. An initial approach to this problem considers a set of low- and high-spectral resolution hyperspectral image pairs and assumes that these images are generated by the same statistical process under a different spectral resolution, and as such, they share the same sparse coding with respect to their corresponding low $\mathbf{D}_l \in \mathbb{R}^{P\times N}$ and high $\mathbf{D}_h \in \mathbb{R}^{M\times N}$ spectral resolution dictionaries [58]. Each low spectral resolution hyperpixel $\mathbf{s}_l \in \mathbb{R}^P$ can, thus, be expressed as a sparse linear combination of elements from a dictionary matrix, $\mathbf{D}_l \in \mathbb{R}^{P\times N}$, composed of hyperpixel atoms from low spectral resolution training datacubes, according to $\mathbf{s}_l = \mathbf{D}_l\mathbf{w}$, where $\mathbf{w} \in \mathbb{R}^N$. Recovery of the sparse coding vector $\mathbf{w}$ is accomplished by solving the ℓ_0-minimization problem

$$\min_{\mathbf{w}} \|\mathbf{w}\|_0 \quad \text{s.t. } \|\mathbf{s}_l - \mathbf{D}_l\mathbf{w}\|_2^2 < \epsilon \tag{1}$$

where ϵ denotes the approximation error modeling the system noise, and $\|\mathbf{w}\|_0 = \#(i|\mathbf{w}_i \neq 0)$ stands for the ℓ_0 pseudonorm counting the number of nonzero elements in a vector. Although the ℓ_0-norm is theoretically the best regularizer for promoting sparsity, it leads to an intractable optimization. This problem is addressed by replacing the ℓ_0-norm by its convex surrogate ℓ_1-norm, where $\ell_1 = \sum_i |\mathbf{w}_i|$, leading to robust solutions and efficient optimization, as follows:

$$\min_{\mathbf{w}} \|\mathbf{w}\|_1 \quad \text{s.t. } \|\mathbf{s}_l - \mathbf{D}_l\mathbf{w}\|_2^2 < \epsilon. \tag{2}$$

The equivalent Lagrangian form of the aforementioned optimization problem is formulated as

$$\min_{\mathbf{w}} \|\mathbf{s}_l - \mathbf{D}_l\mathbf{w}\|_2^2 + \rho\|\mathbf{w}\|_1 \tag{3}$$

where the parameter ρ controls the impact of the sparsity on the solution. To obtain the high-resolution signal, the optimal sparse code $\mathbf{w}^\star$ from (3), is directly mapped onto the high-spectral resolution dictionary $\mathbf{D}_h \in \mathbb{R}^{M\times N}$, to synthesize the high-spectral resolution hyperpixel, according to $\mathbf{s}_h = \mathbf{D}_h\mathbf{w}^\star$. The concatenation of all the recovered high-spectral resolution hyperpixels synthesizes the high-spectral resolution 3-D hypercube, as shown in Fig. 2.

The two main challenges pertaining to the estimation of the high-spectral resolution hypercubes are related to: 1) the sufficient sparsity measure for the sparse coding vector $\mathbf{w}$ and 2) the proper construction of the low- and high-spectral resolution dictionary matrices, $\mathbf{D}_l$ and $\mathbf{D}_h$, to efficiently sparsify the input signals.

IV. COUPLED DICTIONARY LEARNING

Generally, coupled dictionary learning refers to the problem of identifying two dictionary matrices standing for two different signal representations, for instance, low- and high-resolution RGB images [50], blurry and clean images [59], or low-light and well-illuminated scenes [60]. A straightforward strategy to create low- and high-spectral resolution dictionaries is to randomly sample multiple hyperpixels extracted from corresponding low- and high-spectral resolution training scenes and to use this random selection as the sparsifying dictionary. However, this strategy is extremely inefficient since no information regarding the generative power of these examples is known. Alternatively, a joint feature space can be constructed and a single dictionary learning scheme, such as the K-singular value decomposition (K-SVD) [61], can be considered [58].

The proposed SCDL algorithm relies on generating coupled dictionaries which jointly encode two coupled feature spaces, namely, the observation low spectral resolution $\mathbf{S}_l \in \mathbb{R}^{P\times K}$, and the latent high-spectral resolution $\mathbf{S}_h \in \mathbb{R}^{M\times K}$. The main task is to find a coupled dictionary pair $\mathbf{D}_l$ and $\mathbf{D}_h$ for the spaces $\mathbf{S}_l$ and $\mathbf{S}_h$, respectively. Formally, the ideal pair of coupled dictionaries $\mathbf{D}_l$ and $\mathbf{D}_h$ can be estimated by solving the following set of sparse decompositions:

$$\begin{aligned}\underset{\mathbf{D}_h,\mathbf{D}_\ell,\mathbf{W}_h,\mathbf{W}_\ell}{\operatorname{argmin}} \quad & \|\mathbf{S}_h - \mathbf{D}_h\mathbf{W}_h\|_F^2 + \|\mathbf{S}_l - \mathbf{D}_\ell\mathbf{W}_\ell\|_F^2 \\ & + \lambda_h\|\mathbf{W}_h\|_1 + \lambda_\ell\ \|\mathbf{W}_\ell\|_1 \\ \text{s.t. } \mathbf{W}_h = \mathbf{W}_\ell, \quad & \|\mathbf{D}_h(:,i)\|_2 \le 1, \ \|\mathbf{D}_\ell(:,i)\|_2 \le 1\end{aligned} \tag{4}$$

where $\mathbf{W}_l$ is the sparse coefficient matrix corresponding to the low spectral resolution feature space, $\mathbf{W}_h$ stands for the sparse coefficient matrix corresponding to the high-spectral resolution feature space, while λ_h and λ_l denote the parameters that control the sparsity penalty for each individual subproblem.

Coupled dictionary learning considers the joint identification of two dictionary matrices $\mathbf{D}_h$, $\mathbf{D}_l$, representing the coupled feature spaces $\mathbf{S}_h$ and $\mathbf{S}_l$, such that both hyperpixels

$\mathbf{s}_h(i) \in \mathbf{S}_h$ and $\mathbf{s}_l(i) \in \mathbf{S}_l$ share exactly the same sparse coding vector in terms of $\mathbf{D}_h$ and $\mathbf{D}_l$, respectively. A straightforward approach is to concatenate the coupled feature spaces and utilize a common SR $\mathbf{W}$, able to reconstruct both $\mathbf{S}_h$ and $\mathbf{S}_l$, by solving the optimization problem

$$\begin{aligned}&\underset{\mathbf{D},\mathbf{W}}{\operatorname{argmin}} \|\bar{\mathbf{S}} - \bar{\mathbf{D}}\mathbf{W}\|_F^2 + \lambda\|\mathbf{W}\|_1\\ &\text{s.t. } \|\bar{\mathbf{D}}(:,i)\|_2^2 \le 1, \quad i = \{1, \ldots, K\}\end{aligned} \tag{5}$$

where $\bar{\mathbf{S}} = \begin{bmatrix}\mathbf{S}_h\\ \mathbf{S}_l\end{bmatrix}$, $\bar{\mathbf{D}} = \begin{bmatrix}\mathbf{D}_h\\ \mathbf{D}_\ell\end{bmatrix}$, and λ is the sparsity regularization term corresponding to the coupled feature space. In addition to sparsity, the elements of the learned dictionary are also normalized to unit ℓ_2-norm. As a result, the problem posed in (5) is converted into a standard, single-sparse decomposition problem, that can be efficiently solved via existing dictionary learning algorithms, such as the K-SVD [61]. However, such a strategy is optimal only in the concatenated feature space, and not in the individual feature spaces of $\mathbf{S}_h$ and $\mathbf{S}_\ell$. Thus, when presented only with examples from $\mathbf{S}_l$, the generated low-spectral resolution dictionary $\mathbf{D}_l^*$ may adhere to different optimal space coding compared to $\bar{\mathbf{D}}$.

A major limitation of strategies relying either on a random collection of signal pairs or on a single dictionary learning is their inability to guarantee that the same sparse coding can be independently utilized by the different signal resolutions. In other words, during the application of a spectral superresolution process, only low-resolution signals are available. Thus, although one could consider only the low-resolution part of a learned dictionary, no constraints on the optimality of the identified sparse codes exist when high-resolution signals are considered. To overcome this limitation, we propose learning a compact dictionary from low- and high-spectral resolution hyperpixels.

We introduce a computationally efficient *coupled dictionary learning* technique, based on the ADMMs [21], [22], [62], [63] formulation, which converts the constrained dictionary learning problem posed in (5) into an unconstrained version which can be efficiently solved via alternating minimizations. Formally, we consider the observation signals, $\mathbf{S}_\ell = \{\mathbf{s}_\ell\}_{i=1}^N$, and $\mathbf{S}_h = \{\mathbf{s}_h\}_{i=1}^P$. The main task of coupled dictionary learning is to recover both the dictionaries $\mathbf{D}_h$ and $\mathbf{D}_\ell$ and their corresponding sparse codes $\mathbf{W}_h$ and $\mathbf{W}_\ell$, under the constraint, $\mathbf{W}_h = \mathbf{W}_\ell$, by solving the following individual sparse matrix decomposition problems:

$$\begin{aligned}&\underset{\mathbf{D}_h,\mathbf{W}_h}{\operatorname{argmin}} \|\mathbf{D}_h\mathbf{W}_h - \mathbf{S}_h\|_F^2 + \lambda_h\|\mathbf{W}_h\|_1, \|\mathbf{D}_h(:,i)\|_2^2 \le 1\\ &\underset{\mathbf{D}_\ell,\mathbf{W}_\ell}{\operatorname{argmin}} \|\mathbf{D}_\ell\mathbf{W}_\ell - \mathbf{S}_\ell\|_F^2 + \lambda_\ell\|\mathbf{W}_\ell\|_1, \|\mathbf{D}_\ell(:,i)\|_2^2 \le 1.\end{aligned} \tag{6}$$

To apply the ADMM scheme in our spectral dictionary learning procedure, we reformulate the ℓ_1-minimization problem in (6) as

$$\begin{aligned}\min_{\mathbf{D}_h,\mathbf{W}_h,\mathbf{D}_\ell,\mathbf{W}_\ell} \quad & \|\mathbf{S}_h - \mathbf{D}_h\mathbf{W}_h\|_F^2 + \|\mathbf{S}_\ell - \mathbf{D}_\ell\mathbf{W}_\ell\|_F^2\\ & + \lambda_\ell\|\mathbf{Q}\|_1 + \lambda_h\|\mathbf{P}\|_1\\ \text{s.t. } & \mathbf{P} - \mathbf{W}_h = 0, \quad \mathbf{Q} - \mathbf{W}_\ell = 0, \ \mathbf{W}_h - \mathbf{W}_\ell = 0\\ & \|\mathbf{D}_h(:,i)\|_2^2 \le 1, \quad \|\mathbf{D}_\ell(:,i)\|_2^2 \le 1.\end{aligned} \tag{7}$$

Consequently, in comparison with the traditional coupled dictionary learning strategies, we impose the constraint that the two SRs $\mathbf{W}_\ell$ and $\mathbf{W}_h$ of the coupled feature spaces, $\mathbf{S}_\ell$ and $\mathbf{S}_h$, should be the same directly into the optimization. The ADMM scheme takes into account the separate structure of each variable in (7), relying on the minimization of its unconstrained augmented Lagrangian function

$$\begin{aligned}&\mathcal{L}(\mathbf{D}_h, \mathbf{D}_\ell, \mathbf{W}_h, \mathbf{W}_\ell, \mathbf{P}, \mathbf{Q}, Y_1, Y_2, Y_3)\\ &\quad = \frac{1}{2}\|\mathbf{D}_h\mathbf{W}_h - \mathbf{S}_h\|_F^2 + \frac{1}{2}\|\mathbf{D}_\ell\mathbf{W}_\ell - \mathbf{S}_\ell\|_F^2\\ &\qquad + \lambda_h\|\mathbf{P}\|_1 + \lambda_\ell\|\mathbf{Q}\|_1 + \langle Y_1, \mathbf{P} - \mathbf{W}_h\rangle\\ &\qquad + \langle Y_2, \mathbf{Q} - \mathbf{W}_\ell\rangle + \langle Y_3, \mathbf{W}_h - \mathbf{W}_\ell\rangle\\ &\qquad + \frac{c_1}{2}\|\mathbf{P} - \mathbf{W}_h\|_F^2 + \frac{c_2}{2}\|\mathbf{Q} - \mathbf{W}_\ell\|_F^2 + \frac{c_3}{2}\|\mathbf{W}_h - \mathbf{W}_\ell\|_F^2\end{aligned} \tag{8}$$

where $\mathbf{Y}_1$, $\mathbf{Y}_2$, and $\mathbf{Y}_3$ stand for the Lagrange multiplier matrices, while $c_1 > 0, c_2 > 0$, and $c_3 > 0$ denote the step-size parameters. Following the general algorithmic strategy of the ADMM scheme, we seek for the stationary point solving iteratively for each one of the variables while keeping the others fixed. As a result, we create the following sequence of update rules.

1) *Sparse Coding Subproblems*: For minimizing the augmented Lagrangian function with respect to the sparse coding matrices $\mathbf{W}_l$ and $\mathbf{W}_h$, we solve the individual sparse coding problems

$$\begin{aligned}\mathbf{W}_h^\star &= \underset{\mathbf{W}_h}{\operatorname{argmin}}\ \mathcal{L}\\ \mathbf{W}_\ell^\star &= \underset{\mathbf{W}_\ell}{\operatorname{argmin}}\ \mathcal{L}.\end{aligned} \tag{9}$$

Setting $\nabla_{\mathbf{W}_h}\mathcal{L} = \nabla_{\mathbf{W}_\ell}\mathcal{L} = 0$, the subproblems admit closed-form solutions

$$\begin{aligned}\mathbf{W}_h &= \left(\mathbf{D}_h^T \cdot \mathbf{D}_h + c_1 \cdot I + c_3 \cdot I\right)^{-1}\\ &\quad \cdot \left(\mathbf{D}_h^T \cdot \mathbf{S}_h + Y_1 - Y_3 + c_1 \cdot \mathbf{P} + c_3 \cdot \mathbf{W}_\ell\right)\\ \mathbf{W}_\ell &= \left(\mathbf{D}_\ell^T \cdot \mathbf{D}_\ell + c_2 \cdot I + c_3 \cdot I\right)^{-1}\\ &\quad \cdot \left(\mathbf{D}_l^T \cdot \mathbf{S}_\ell + Y_2 + Y_3 + c_2 \cdot \mathbf{Q} + c_3 \cdot \mathbf{W}_h\right).\end{aligned} \tag{10}$$

2) *Subproblems* **P** and **Q**

$$\begin{aligned}&\nabla_{\mathbf{P}}\left(\lambda_h\|\mathbf{P}\|_1 + \langle Y_1, \mathbf{P} - \mathbf{W}_h\rangle + \frac{c_1}{2}\|\mathbf{P} - \mathbf{W}_h\|_F^2\right)\\ &\nabla_{\mathbf{Q}}\left(\lambda_\ell\|\mathbf{Q}\|_1 + \langle Y_2, \mathbf{Q} - \mathbf{W}_\ell\rangle + \frac{c_2}{2}\|\mathbf{Q} - \mathbf{W}_\ell\|_F^2\right).\end{aligned} \tag{11}$$

Setting $\nabla_{\mathbf{P}}\mathcal{L} = \nabla_{\mathbf{Q}}\mathcal{L} = 0$, the subproblems can be reformulated as

$$\begin{aligned}\mathbf{P} &= S_{\lambda_h}\left(\left|\mathbf{W}_h - \frac{Y_1}{c_1}\right|\right)\\ \mathbf{Q} &= S_{\lambda_\ell}\left(\left|\mathbf{W}_\ell - \frac{Y_2}{c_2}\right|\right)\end{aligned} \tag{12}$$

where S_{λ_h} and S_{λ_ℓ} denote the soft-thresholding operators, defined as

$$S_\lambda(x) = \operatorname{sign}(x) \cdot \max(|x| - \lambda, 0) \tag{13}$$

where $\lambda > 0$ stands for the threshold value.

3) *Subproblems* D_h *and* D_ℓ

For a fixed set of $\mathbf{W}_h$, $\mathbf{W}_\ell$, $\mathbf{P}$, and $\mathbf{Q}$, the dictionaries $\mathbf{D}_h$ and $\mathbf{D}_\ell$ can be updated as

$$\begin{aligned}\mathbf{D}_h^\star &= \underset{\mathbf{D}_h}{\operatorname{argmin}} \mathcal{L}\\ \mathbf{D}_\ell^\star &= \underset{\mathbf{D}_\ell}{\operatorname{argmin}}\ \mathcal{L} \Leftrightarrow \end{aligned} \tag{14}$$

$$\begin{aligned}\nabla_{\mathbf{D}_h}\left(\frac{1}{2}\|\mathbf{S}_h - \mathbf{D}_h\mathbf{W}_h\|_F^2\right) &= -(\mathbf{S}_h - \mathbf{D}_h\mathbf{W}_h)\mathbf{W}_h^T\\ \nabla_{\mathbf{D}_\ell}\left(\frac{1}{2}\|\mathbf{S}_\ell - \mathbf{D}_\ell\mathbf{W}_\ell\|_F^2\right) &= -(\mathbf{S}_\ell - \mathbf{D}_\ell\mathbf{W}_\ell)\mathbf{W}_\ell^T.\end{aligned} \tag{15}$$

Setting $\nabla_{\mathbf{D}_h} = \nabla_{\mathbf{D}_\ell} = 0$, the high- and the low-spectral resolution dictionaries are updated column by column adhering to the following iterative scheme:

$$\begin{aligned}\phi_h &= \mathbf{W}_h(j,:) \cdot \mathbf{W}_h(j,:)^T\\ \phi_\ell &= \mathbf{W}_\ell(j,:) \cdot \mathbf{W}_\ell(j,:)^T\end{aligned} \tag{16}$$

and

$$\begin{aligned}\mathbf{D}_h^{(k+1)}(:,j) &= \mathbf{D}_h(:,j)^{(k)}(:,j) + \frac{\mathbf{S}_h \cdot \mathbf{W}_h(j,:)}{\phi_h + \delta}\\ \mathbf{D}_\ell^{(k+1)}(:,j) &= \mathbf{D}_\ell(:,j)^{(k)}(:,j) + \frac{\mathbf{S}_\ell \cdot \mathbf{W}_\ell(j,:)}{\phi_\ell + \delta}\end{aligned} \tag{17}$$

where k denotes the number of iterations, δ stands for a small regularization factor, while $\mathbf{D}_h(:,j)$ and $\mathbf{D}_\ell(:,j)$ represent the jth column of $\mathbf{D}_h$ and $\mathbf{D}_\ell$, respectively. Finally, the Lagrangian multiplier matrices are updated as

$$\begin{aligned}Y_1^{(k+1)} &= Y_1^{(k)} + c_1(\mathbf{P} - \mathbf{W}_h)\\ Y_2^{(k+1)} &= Y_2^{(k)} + c_2(\mathbf{Q} - \mathbf{W}_l)\\ Y_3^{(k+1)} &= Y_3^{(k)} + c_3(\mathbf{W}_h - \mathbf{W}_l).\end{aligned} \tag{18}$$

In our setup, we set $c_1 = c_3 = 0.8$ and $c_2 = 0.6$. The derivations of the individual subproblems for the proposed SCDL-ADMM-based dictionary learning scheme are shown in the Appendix. The overall algorithm for learning the coupled dictionaries, which correspond to the high- and the low-spectral resolution feature spaces, is summarized in **Algorithm 1**.

Algorithm 1 Spectral Coupled Dictionary Learning

```
Input: training examples $\mathbf{S}_h$ and $\mathbf{S}_l$, number of iterations K and step size parameters $c_1, c_2, c_3$.
Initialize: $\mathbf{D}_h \in \mathbb{R}^{M\times N}$ and $\mathbf{D}_l \in \mathbb{R}^{P\times N}$ are initialized by a random selection of the columns of $\mathbf{S}_h$ and $\mathbf{S}_l$ with normalization; Initialize Lagrange multiplier matrices $\mathbf{Y}_1 = \mathbf{Y}_2 = \mathbf{Y}_3 = \mathbf{0}$.
for $k = 1, \cdots, K$ do
    1) Update $\mathbf{W}_h$ and $\mathbf{W}_\ell$ via (10)
    2) Update $\mathbf{P}$ and $\mathbf{Q}$ via (12)
    3) for $j = 1, \cdots, N$ do
        a) Update $\phi_h$ and $\phi_l$ via (16)
        b) Update the two dictionaries $\mathbf{D}_h$ and $\mathbf{D}_l$ column by column via (17)
    end
        a) Normalize $\mathbf{D}_h$ and $\mathbf{D}_l$ between [0, 1]
        b) Update Lagrange multiplier matrices $Y_1$, $Y_2$ and $Y_3$ via (18)
end
```

V. Experimental Evaluation

In this section, we evaluate the performance of the proposed SCDL scheme when applied to the spectral super-resolution of hyperspectral imagery in terms of the quality of the estimated high-spectral resolution hypercubes. The performance is quantified on both synthetic and real remote sensing data. Specifically, we have experimented with multispectral and hyperspectral data acquired by: 1) NASA's EO-1 Hyperion [13] sensor; 2) NASA's MODIS sensor [14]; 3) NASA's Landsat-8 Operational Land Imager (OLI) instrument [64]; and 4) ESA's Sentinel-2 satellite [19].

The Hyperion sensor resolves 224 spectral bands ranging from 0.4 to 2.5 μm, with a 30-m spatial resolution. Due to its high spectral coverage, Hyperion scenes have been widely utilized in the remote sensing community for classification and spectral unmixing purposes [3], [6]. Specifically, we considered several hyperspectral scenes extracted from different Earth locations, acquired on June 16, 2016. We restrict ourselves to the 96 calibrated and high-resolution spectral bands in the visible (VIS) and near-infrared (VNIR) spectrum range, namely, (B9:B16, B18:B25, B28:B33, B42:B45, B49:B57, B77:B105, B106:B115, B141:B160, and B191:B192). In addition, the MODIS [14] sensor acquires 36 spectral bands ranging between 0.4 and 14.4 μm, at varying spatial resolutions (2 bands at 250 m, 5 bands at 500 m, and 29 bands at 1 km). Finally, we considered the multispectral data scanned by the same region and extracted by the OLI sensor of the Landsat-8 satellite and the Sentinel-2 sensor, on September 17, 2017. The OLI sensor collects data at a 30-m spatial resolution and resolves 8 spectral bands in the VNIR and in the shortwave infrared (SWIR) spectral regions of the electromagnetic spectrum, plus an additional panchromatic band at 15-m spatial resolution, resulting into 9 spectral bands. On the other hand, the Sentinel-2 satellite provides high spatial, spectral, and temporal-resolution multispectral scenes, while it ensures the continuity of Landsat's observations. Sentinel-2 covers the VNIR and the SWIR spectral regions, resolving 13 spectral observations. Fig. 3 depicts the spectral response functions of the Sentinel-2 and the Landsat-8 multispectral sensors, where one can observe the overlapping and the nonoverlapping spectral bands between the two different instruments.

A. Implementation and Evaluation Metrics

In order to validate the performance of the hyperspectral image enhancmenet algorithms, we employ the *peak signal-to-noise ratio* (PSNR) metric [65] given as

$$\text{PSNR} = 10\log_{10}\left[L_{\max}^2/\text{MSE}(x,y,b)\right]$$

where L is the maximum pixel value of the scene, b denotes the spectral dimension, and MSE stands for the mean square

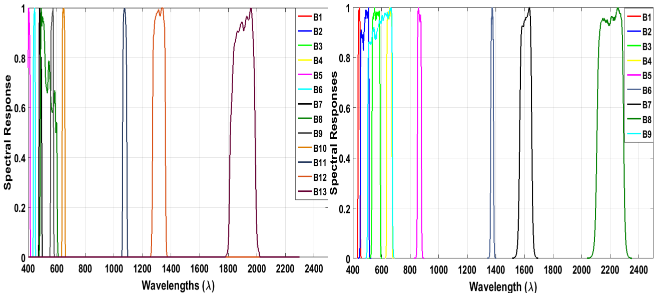

(a) (b)

Fig. 3. Spectral signatures of the Sentinel-2 and the Landsat-8 multispectral sensors. (a) Spectral Responses of Sentinel-2. (b) Spectral Responses of Landsat-8.

error, defined as

$$\mathrm{MSE}(x, y, b) = \frac{\sum_{x,y,b}[\mathbf{S}_{h_{(x,y,b)}} - \mathbf{S}_{l_{(x,y,b)}}]^2}{n_x n_y b} \tag{19}$$

where x and y denote the spatial dimensions of the input and the synthesized images $\mathbf{S}_l$ and $\mathbf{S}_h$. Consequently, we evaluate the PSNR error metric across all the recovered spectral bands.

In addition, we evaluate the performance of the recovered hyperspectral images in terms of the *spectral angular mapper* (SAM) [66]–[68]. This metric determines the *spectral similarity* between two spectra by calculating the angle between the corresponding vectors of the testing and the reference hypercubes, formulated as

$$\theta = \cos^{-1}\left(\frac{\sum_{i=1}^{N} t_i r_i}{\sqrt{\sum_{i=1}^{N} t_i^2}\sqrt{\sum_{i=1}^{N} r_i^2}}\right) \tag{20}$$

where t stands for the testing spectrum, r refers to the reference spectrum, while N denotes the number of the available spectral bands. Small values of SAM indicate a high similarity between the compared spectral vectors.

Regarding the dictionary training phase, pairs of low- and high-spectral resolution dictionaries were prepared, one for each sensor data set. In all cases, we utilized 10 training hypercubes from which 10^5 training hyperpixels were randomly extracted. In the experimental results section, we further investigate and show graphically the impact of the dictionary size on the reconstruction performance.

VI. EXPERIMENTAL RESULTS

A. Synthetic Data Scenario

Concerning the synthetic data case, we use the hyperspectral data acquired by NASA's EO-1 Hyperion satellite [13]. Instead of using predefined subsampling factors for synthesizing the low-spectral resolution data cubes [58], we consider a more realistic scenario of spectral downsampling based on the spectral profiles of low spectral resolution sensors. Specifically, we first construct the spectral calibration data, i.e., the spectral profiles (downsampling) matrix that represents the relation between the two different representations, the high and the low spectral resolutions.

In order to generate the corresponding low-spectral resolution hypercubes, we consider the following scenario: for each spectral observation of Hyperion, we find the corresponding wavelength value of another (target) instrument that acquires hyperspectral data with a limited spectral resolution. Formally, let $\mathbf{s}_h \in \mathbb{R}^P$ be a high-spectral resolution hyperpixel, acquired with P spectral bands, while $\mathbf{B} \in \mathbb{R}^{P \times M}$ stands for the spectral profiles (downsampling) matrix, representing the spectral calibration data, and M denotes the number of limited spectral observations. The corresponding low spectral resolution hyperpixel, $\mathbf{s}_l \in \mathbb{R}^M$, is constructed as $\mathbf{s}_l = \mathbf{B}^T \mathbf{s}_h$. This procedure is performed for every spectral observation of the low-spectral resolution instrument.

In this paper, we have experimented with ESA's Sentinel-2 and NASA's MODIS spectral response functions, and thus, we have created two different spectral downsampling matrices, one for each acquisition scenario. Concerning the Sentinel-2 satellite case, we considered the corresponding spectral observations that overlap with the calibrated and high-resolution Hyperion spectral bands. Specifically, the overlapping spectral bands among the two instruments are (B1:B4, B7, B8, and B12). The spectral calibration data for the Sentinel acquisition scenario form a matrix of size 96 × 7. Consequently, we reconstruct the 96 high-resolution bands of Hyperion from only 7 spectral observations of the Sentinel-2 sensor. Likewise, we used the spectral profiles of the multispectral MODIS sensor to synthesize the low-spectral resolution hypercubes. For each Hyperion spectral observation, we find the corresponding wavelength values of the MODIS sensor. Similarly, the overlapping spectral observations between the Hyperion and the MODIS sensors are B1:B6, B9:B14, and B16:B19, resulting in 14 spectral observations for the low-resolution case. As a result, the spectral downsampling matrix is of size 96 × 14. Fig. 4 illustrates this spectral subsampling process.

In order to validate the merits of the proposed spectral superresolution scheme, we first compare the synthesized 3-D hypercubes against the ground truth cubes and against three state-of-art techniques, namely: 1) the baseline approach of cubic interpolation among the available spectral bands; 2) the sparse-based method of spectral superresolution using the naive scenario of K-SVD coupled dictionary learning [58]; and 3) the reweighted ℓ_1 spatial filtering (RWL1-SF) algorithm [54], [55] that learns a single dictionary of spectral signatures in order to decompose the spectral response of each hyperpixel. To achieve a fair comparison with the K-SVD coupled dictionary learning technique, we utilize the same number of atoms for dictionary learning and the same sparsity constraints. For the reweighted ℓ_1 spatial filtering scheme, we chose the parameters that achieve the best possible reconstruction. In the following paragraphs, the performance of the competing spectral superresolution techniques is assessed using the quantitative evaluation metrics PSNR and SAM and by qualitative visual inspection.

Figs. 5 and 6 show representative bands from the reconstructed hypercubes obtained using the proposed SCDL method when applied on Cube 1 of the EO1H1860262006099110KF hyperspectral scene. In both

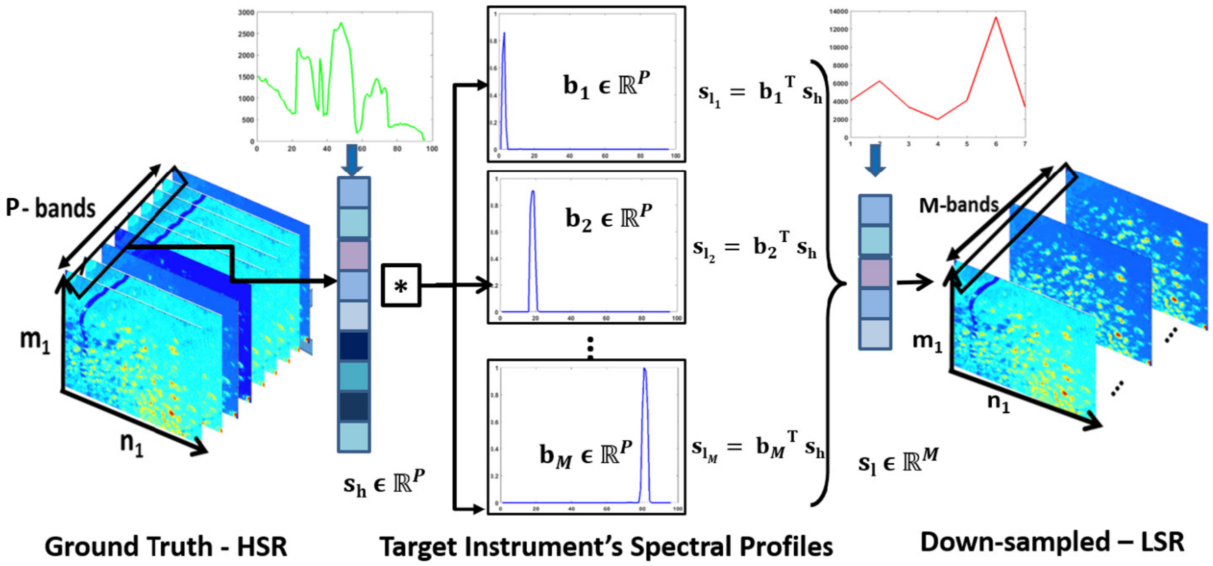

Fig. 4. Hyperspectral data downsampling process. High-resolution hyperpixels are modulated by the spectral calibration data in order to synthesize the corresponding realistic low-spectral resolution hyperpixels. The spectral profiles (downsampling) matrix provides the corresponding wavelength values between the two spectral resolution instruments. As illustrated in the figure, each column vector of this matrix is a spectral response function describing the relation between the two satellite sensors.

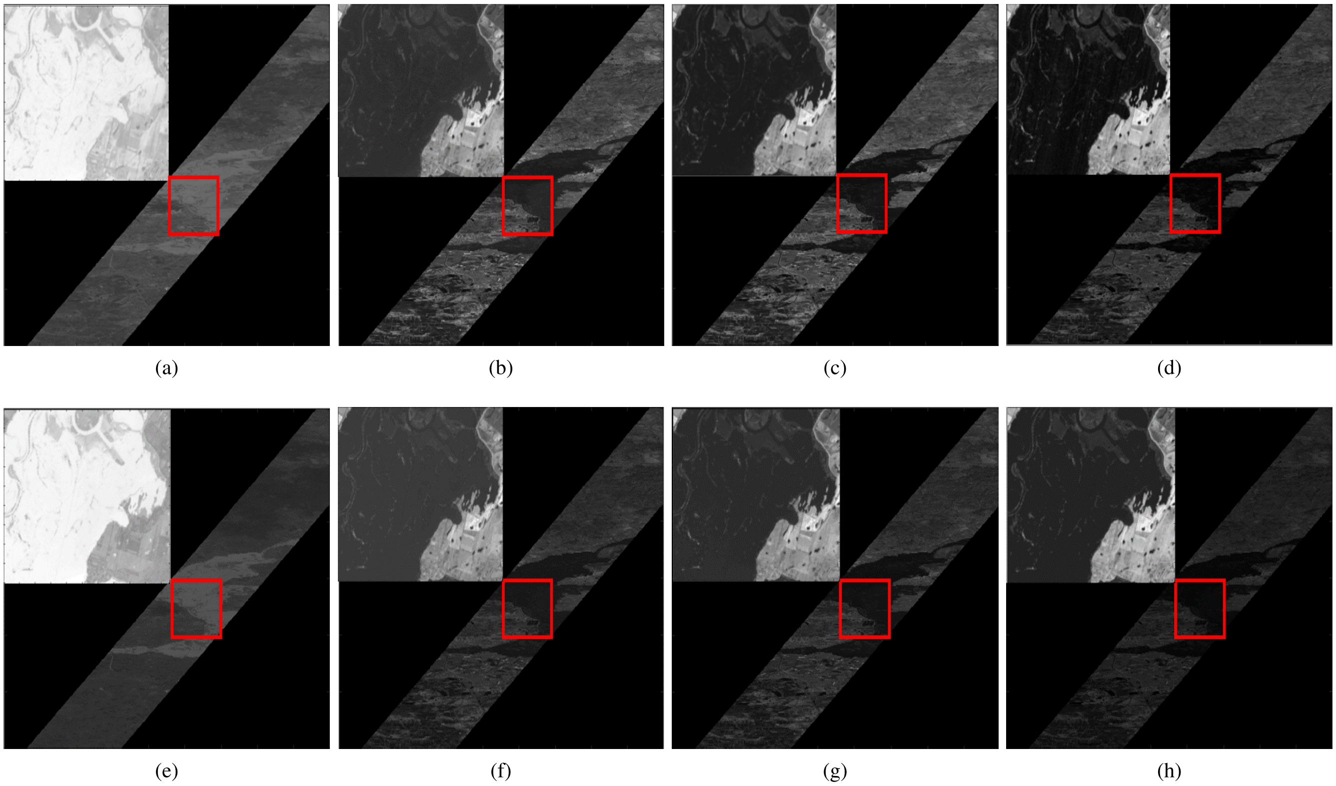
(a) (b) (c) (d)

(e) (f) (g) (h)

Fig. 5. Sentinel to Hyperion spectral band reconstruction using SCDL. Full spectrum is composed of 96 bands in the VIS–NIR region, and the full resolution hypercube is estimated from 7 input spectral bands. In this simulation, we illustrate four characteristic spectral bands of the proposed algorithm's reconstruction. Specifically, we demonstrate the 10th, 25th, 30th, and 50th spectral observations. Each spectral band corresponds to a different wavelength range. Consequently, we may notice the subtle differences among the spectral bands. In addition, we observe that under real-life conditions, the proposed SCDL scheme produces a significant quality improvement operating in satellite hyperspectral imagery. (a) Ground truth 10th band. (b) Ground truth 25th band. (c) Ground truth 30th band. (d) Ground truth 50th band. (e) 10th band, PSNR: 47.87 dB. (f) 25th band, PSNR: 46.54 dB. (g) 30th band, PSNR: 44.32 dB. (h) 50th band, PSNR: 46.81 dB.

figures, we employ the spectral downsampling for the Sentinel-2 instrument, and thus, we reconstruct the full spectrum composed of 96 spectral bands from only 7 available spectral observations. Fig. 5 demonstrates four characteristic spectral bands from a full-spatial resolution hypercube ($3000 \times 900 \times 96$), along with a specific region of interest. For this purpose, we depict the reconstructed 10th, 25th, 30th, and 50th spectral bands, along with their ground

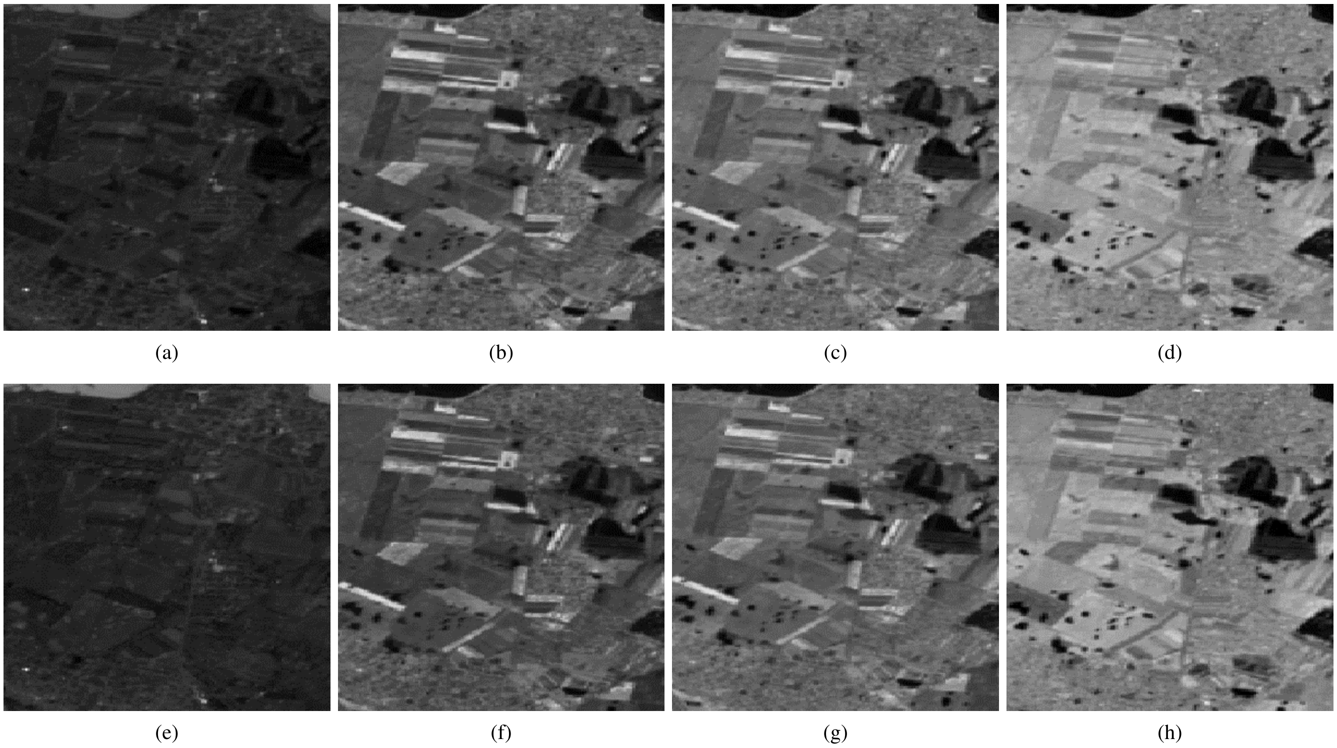

Fig. 6. Sentinel to Hyperion cropped area reconstruction: In this experiment, we investigate the performance of our SCDL scheme when applied on a cropped area of Cube 1 (EO1H1860262006099110KF), with a spatial resolution of (271 × 184) pixels. (Top row) Original spectral bands. (Bottom row) SCDL reconstructed spectral bands. The full spectrum is composed of 96 bands, while the available spectral observations are only 7. In this experiment, we demonstrate four characteristic spectral bands, each one corresponding to a different value of the spectrum. (a) Ground truth 10th band. (b) Ground truth 30th band. (c) Ground truth 50th band. (d) Ground truth 90th band. (e) 10th band, PSNR: 38.97 dB. (f) 30th band, PSNR: 45.26 dB. (g) 50th band, PSNR: 41.23 dB. (h) 90th band, PSNR: 42.84 dB.

truth observations. We chose the specific spectral bands since they are able to discriminate the subtle differences of the reconstructed hypercube. The red-squared area corresponds to the zoomed-in view of the region that is depicted on the top left corner of the images, and it highlights the subtle differences among the various spectral observations. In terms of the PSNR metric, the proposed technique achieves a high performance with respect to the corresponding ground truth measurements, while the mean PSNR across all the reconstructed spectral observations of Cube 1 hyperspectral scene is 46.90 dB. In terms of visual inspection, we note that the reconstructed spectral bands faithfully preserve important image features.

On the other hand, Fig. 6 depicts a cropped-area of the Cube 1 hyperspectral scene. The spatial dimensions of the cropped area are 271×184 pixels. The results highlight the fact that important spatial features of the images, such as the field areas, are correctly synthesized. In this experiment, one can easily notice how different image regions, corresponding to different materials, are reliably estimated. The average PSNR values obtained by the proposed SCDL scheme for the recovery of the full and the cropped 3-D hypercubes are 46.90 and 30.7 dB, respectively.

In Fig. 7, we compare the performance of SCDL with the three state-of-the-art methods when applied on the cropped (271 × 184) area of Cube 1 (EO1H1860262006099110KF). In this experiment, we use Sentinel's spectral profiles in order to downsample the high-spectral resolution hyperspectral data, and thus, we recover the full spectrum, composed of 96 spectral bands, from only 7 input spectral observations. We observe that the RWL1-SF and the K-SVD techniques are not able to reconstruct significant features such as the road areas at the top of the scenes. One may notice the subtle differences among the various techniques in the marked red-squared region of interest. The reweighted spatial filtering technique introduces severe artifacts in the reconstruction. In contrast, the K-SVD spectral superresolution approach provides a smoother recovery compared to RWL1-SF, but not as good as the proposed SCDL scheme, which achieves the highest accuracy with the ground truth 3-D hypercube, both visually and quantitatively, in terms of the attained evaluation metrics. The PSNR values obtained by RWL1-SF, K-SVD, and SCDL are 25.72, 26.85, and 30.7 dB, respectively. In terms of the SAM error metric, the RWL1-SF algorithm achieves 0.188, while the K-SVD spectral superresolution approach achieves 0.035. In contrast, the proposed SCDL scheme achieves an even smaller SAM value, 0.027, indicating a higher similarity among the reconstructed and ground truth hypercubes.

Another indicative set of reconstruction results is depicted in Fig. 8, where the performance of the various methods is evaluated on a cropped region (400 × 200) of hyperspectral Cube 3 (EO1H1900512016017110KF). In this experiment, we used MODIS spectral profiles to synthesize the low-spectral resolution part. Hence, the full 96 spectral bands

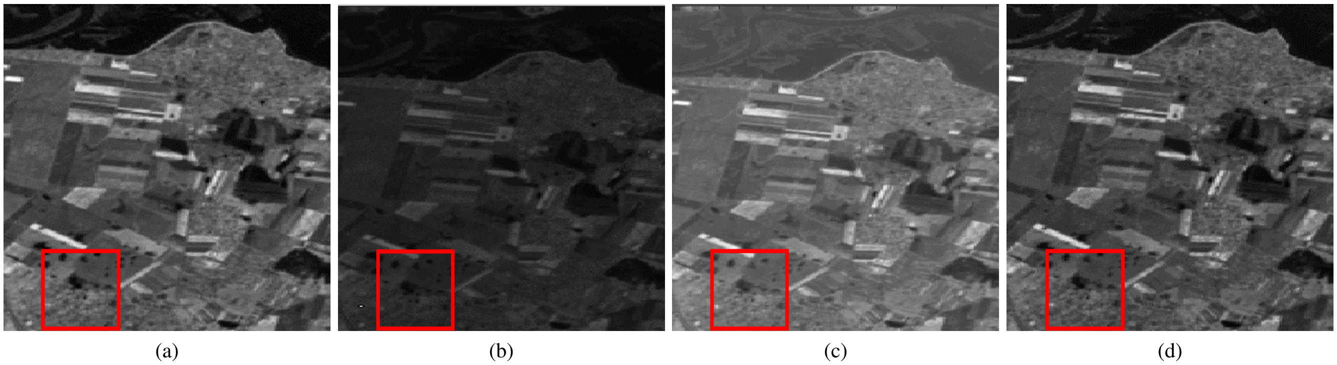

Fig. 7. Cube 1 (EO1H1860262006099110KF). Comparison with the state of the art. In this experiment, we consider the 30th band of Hyperion's hyperspectral scene. We recover the full hypercube from only 7 input spectral observations, using Sentinel's spectral profiles matrix. The SCDL scheme outperforms the state-of-the-art approaches both visually and in terms of the PSNR error metric. (a) Ground Truth 30th Band. (b) RWL1-SF PSNR: 25.72 dB, SAM: 0.188. (c) SSR-K-SVD, PSNR: 26.85 dB, SAM: 0.035. (d) SCDL, PSNR: 30.7 dB, SAM: 0.027.

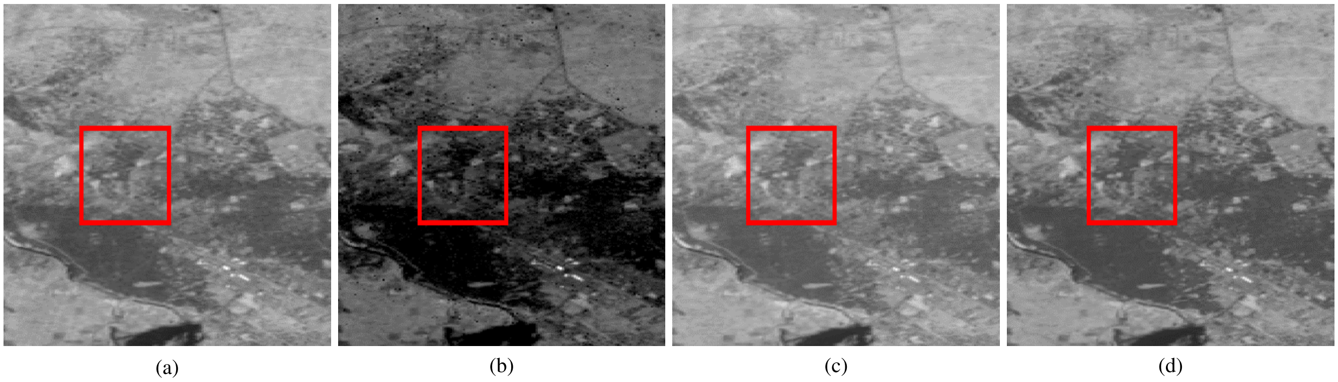

Fig. 8. Cube 3 (EO1H1900512016017110KF). Comparison with state of the art. In this experiment, we use MODIS spectral profiles in order to synthesize the low-spectral resolution part. The full spectrum is composed of 96 bands in the VIS–NIR region, while the full resolution hypercube is estimated from 14 input spectral bands. We observe that under real-life conditions, the proposed SCDL method has a better performance than both RWL1-SF and K-SVD. (a) Ground Truth 53th Band. (b) RWL1-SF, 22.23 dB, SAM: 0.103. (c) K-SVD, PSNR: 30.22 dB, SAM: 0.035. (d) SCDL, PSNR: 31.83 dB, SAM: 0.021.

spectrum is recovered from 14 spectral observations. Fig. 8 illustrates the 53rd spectral band. Visual observation reveals that the RWL1-SF technique introduces severe artifacts at the high-spatial-frequency regions such as the marked red-squared area. On the other hand, K-SVD produces a smooth spectral representation of the scene without introducing spectral and noisy effects. Again, the proposed SCDL technique provides a more accurate and smooth approximation of the ground truth, revealing significant details over all regions of this challenging scene. In terms of the PSNR metric, the proposed scheme outperforms the other methods by achieving 31.83 dB, as compared to 22.23 and 30.22 dB, obtained by RWL1-SF and K-SVD, respectively. Similar observations can be made for the SAM index, where the proposed algorithm attains the smallest value of 0.021, better than the RWL1-SF (0.103) and the K-SVD (0.035).

Fig. 9 illustrates the performance of the various techniques when applied on hyperspectral Cube 4 (EO1H1180652016162110KF). Specifically, we depict a cropped (400 × 200) region of the 70th acquired spectral band. In this scenario, we use the MODIS instrument spectral profiles and we recover the 96-band full spectrum from 14 input spectral observations. Outperforming the state-of-the-art approaches that produce noisy reconstructions, SCDL provides a high-resolution hypercube that has a better similarity with the original spectral data, both visually and quantitatively. In addition, in the highlighted red-squared region of interest, one may observe that the proposed scheme faithfully preserves all the important image features. The PSNR values obtained by RWL1-SF, K-SVD, and SCDL are 28.93, 31.64, and 35.81 dB, respectively. In terms of the SAM metric, the proposed SCDL scheme achieves the best (smallest) value of 0.034, followed by K-SVD (0.054) and RWL1-SF (0.120).

A complete set of PSNR and SAM values for all the evaluated techniques applied on several EO-1 Hyperion hyperspectral scenes, of full spatial resolution (3000 × 900), is provided in Table I. In this table, we show the mean reconstruction error and the SAM metric across all the recovered spectral observations. The results demonstrate that the proposed spectral resolution enhancement method outperforms consistently all other competing state-of-the-art techniques on a wide range of challenging hyperspectral scenes.

B. Real Data Scenario

In this paragraph, we evaluate the performance of the proposed SCDL algorithm applied on a real data acquisition

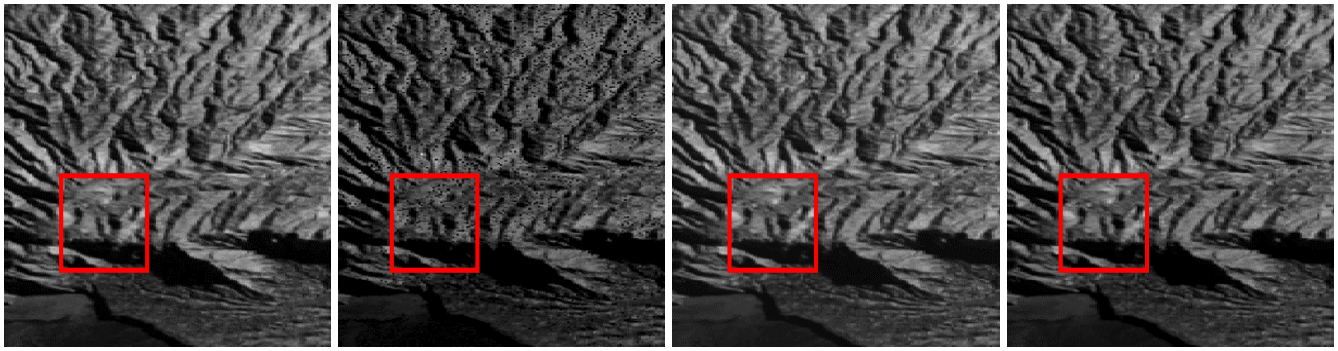
(a) (b) (c) (d)

Fig. 9. Cube 4 (EO1H1180652016162110KF). Comparison with the state of the art. In this experiment, we reconstruct the full spectrum, composed of 96 bands in the VIS–NIR region, from 14 input spectral bands using MODIS spectral profiles matrix. The proposed scheme provides an accurate high-quality reconstruction of the challenging scene, both quantitatively and visually. (a) Ground Truth 70th Band. (b) RWL1-SF, 28.93 dB, SAM:0.120. (c) K-SVD, PSNR:31.64 dB, SAM:0.054. (d) SCDL, PSNR:35.81 dB, SAM:0.034.

TABLE I

QUANTITATIVE PERFORMANCE EVALUATION OF THE PROPOSED SCDL METHOD AGAINST STATE-OF-THE-ART TECHNIQUES IN TERMS OF PSNR (IN DECIBELS) AND SAM ERROR METRICS, USING MODIS AND SENTINEL'S SPECTRAL PROFILES

Image	Scale	Interpolation	RWL1-SF	K-SVD	SCDL
Cube 1 (EO1H1860262006099110KF)	MODIS to Hyperion	33.18, (0.093)	38.60, (0.261)	44.78, (0.034)	**46.40**, (**0.033**)
	Sentinel to Hyperion	37.19, (0.165)	40.57, (0.122)	42.85, (0.031)	**46.90**, (**0.024**)
Cube 2 (EO1H1830332004264110PX)	MODIS to Hyperion	24.66, (0.211)	31.77, (0.224)	32.84, (0.035)	**41.01**, (**0.017**)
	Sentinel to Hyperion	29.14, (0.220)	36.80, (0.203)	38.10, (0.030)	**40.18**, (**0.023**)
Cube 3 (EO1H1900512016017110KF)	MODIS to Hyperion	23.60, (0.105)	28.61, (0.097)	29.63, (0.037)	**38.15**, (**0.024**)
	Sentinel to Hyperion	28.61, (0.215)	35.18, (0.271)	36.26, (0.021)	**40.81**, (**0.019**)
Cube 4 (EO1H1180652016162110KF)	MODIS to Hyperion	33.49, (0.150)	38.50, (0.120)	38.74, (0.063)	**43.92**, (**0.032**)
	Sentinel to Hyperion	30.34, (0.253)	38.12, (0.232)	38.35, (0.050)	**41.15**, (**0.035**)
Cube 5 (EO1H1120822017023110K7)	MODIS to Hyperion	33.84, (0.080)	31.64, (0.236)	40.58, (0.023)	**48.59**, (**0.017**)
	Sentinel to Hyperion	38.72, (0.150)	36.18, (0.277)	46.50, (**0.020**)	**49.40**, (0.030)
Average	MODIS to Hyperion	29.75, (0.127)	33.82, (0.187)	37.31, (0.038)	**43.61**, (**0.024**)
	Sentinel to Hyperion	32.80, (0.200)	37.37, (0.221)	40.41, (0.030)	**43.80**, (**0.026**)

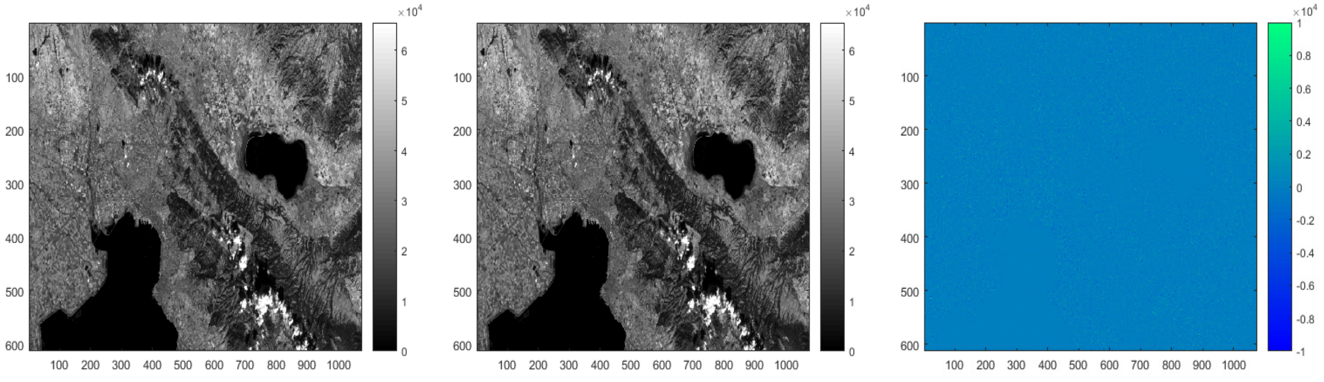

(a) (b) (c)

Fig. 10. Real Data Scenario (North Greece Region). In this experiment, we trained the coupled dictionaries using Sentinel-2 and Landsat-8 data scanned in the same regions. During the testing phase, we consider as input 9 spectral bands of the Landsat-8 multispectral sensor, and we recover the 13 spectral observations of the Sentinel-2 satellite. In order to verify our reconstruction, the output high-spectral resolution hypercube is compared with the ground-truth Sentinel-2 cube. (c) Difference between the reconstructed 12th spectral band and the ground truth 12th band. We observe that the recovered band achieves high similarity with the ground truth spectral band, both visually and in terms of the evaluation metrics (PSNR and SAM). (a) Ground truth 12th band. (b) SCDL, PSNR: 39.75 dB, SAM: 0.034. (c) Difference between SCDL and Ground Truth.

case. Specifically, we considered multispectral data scanned in the same region and extracted by the Landsat-8 OLI sensor and the Sentinel-2 sensor. The challenge is to recover the 13 spectral bands of the Sentinel-2 sensor using as input 9 spectral observations of the Landsat-8 sensor.

Fig. 10 demonstrates the reconstruction result for the 12th spectral band of the Sentinel-2 sensor using the proposed SCDL scheme. Specifically, we illustrate the actual 12th spectral band and its reconstructed version by SCDL. As we may observe, the achieved reconstruction has a high similarity to its corresponding ground truth spectral band, both visually and quantitatively in terms of the PSNR (39.75 dB) and SAM (0.034) error metrics. Fig. 10(c) illustrates the difference between the ground truth and the reconstructed 12th spectral band and clearly demonstrates that the proposed scheme recovers accurately the ground truth spectral observation.

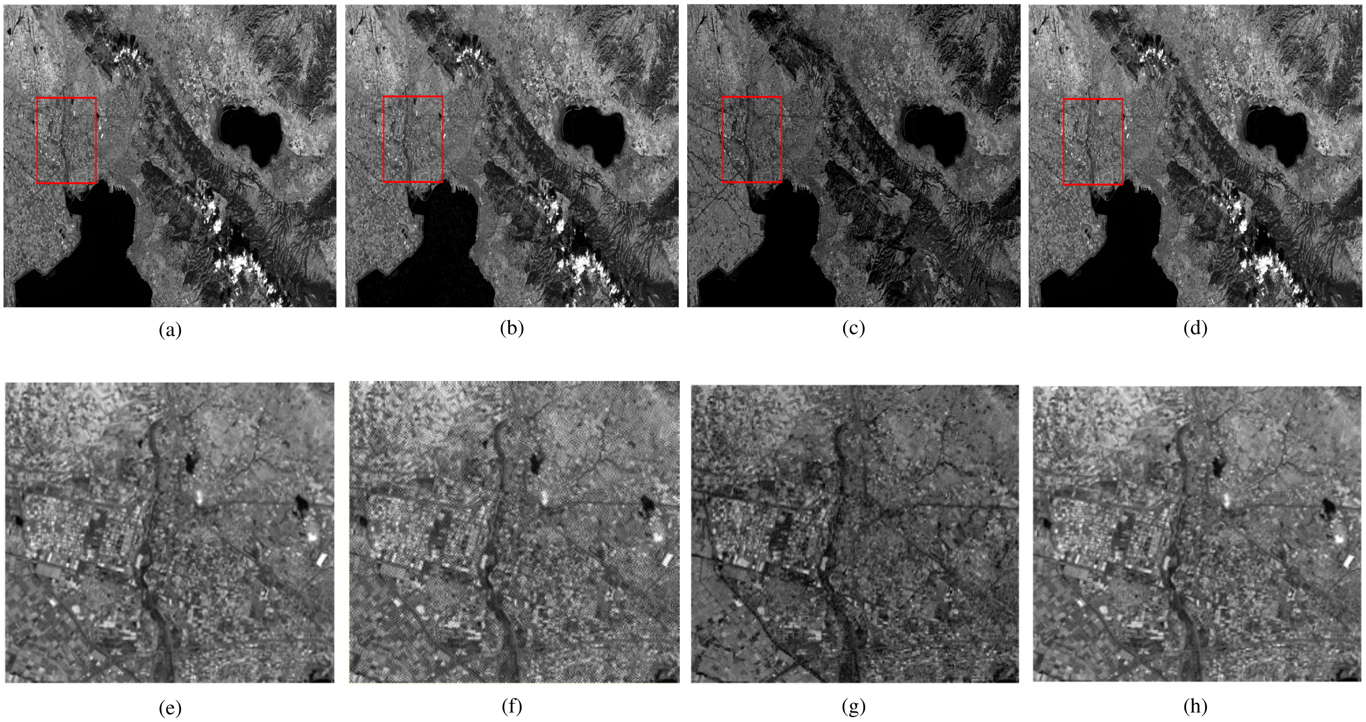
(a) (b) (c) (d)

(e) (f) (g) (h)

Fig. 11. Real Data Acquisition Scenario (North Greece Region). Comparison with state of the art. In this experiment, we depict an example of the proposed algorithm when it is applied to real satellite data. We evaluate the reconstruction quality of the proposed SCDL scheme compared with the state of the art, in the scenario where we recover the 13 spectral bands of Sentinel-2, considering as input 9 spectral observations of Landsat-8. We observe that the proposed algorithm outperforms the state-of-the-art techniques both in terms of the evaluation indexes and visually. In the zoomed-in view of red square regions depicted in the second row, we illustrate the subtle differences among the various techniques. (a) Ground truth 12th band. (b) RWL1-SF, 23.50 dB, SAM: 0.224. (c) K-SVD, PSNR: 33.57 dB, SAM: 0.032. (d) SCDL, PSNR: 39.75 dB, SAM: 0.014. (e) Zoomed-in view—12th Band. (f) Zoomed-in view—RWL1-SF. (g) Zoomed-in view—SSR-K-SVD. (h) Zoomed-in view—SCDL.

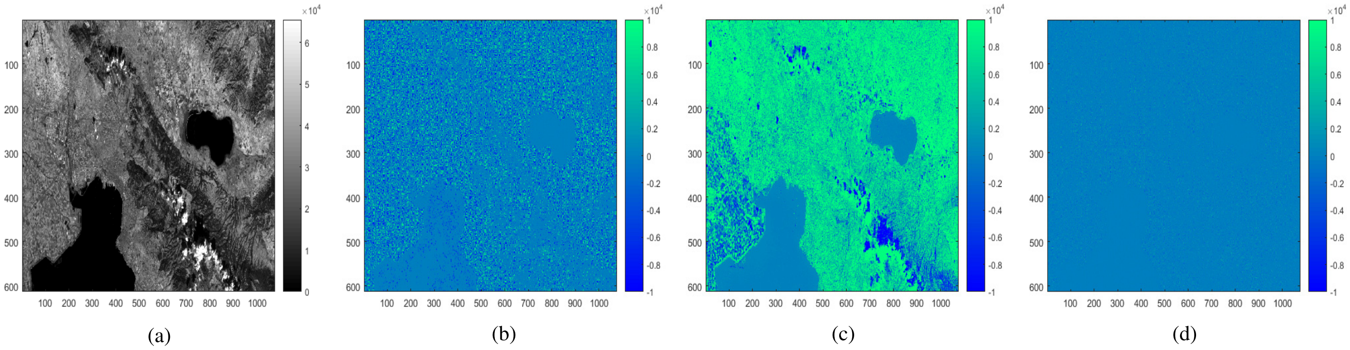

(a) (b) (c) (d)

Fig. 12. Real Data Scenario (North Greece Region). We provide the differences between the 12th band reconstructed by the methods and the ground truth 12th spectral band of the Sentinel-2 sensor. We note that both the RWL1-SF and the K-SVD algorithms produce well-structured difference images, implying a low-quality recovery. In contrast, the proposed technique's difference image with respect to the ground truth denotes an accurate reconstruction of the 12th spectral band. (a) Ground Truth 12th Band. (b) Difference between RWL1-SF and Ground Truth. (c) Difference between SSR-K-SVD and Ground Truth. (d) Difference between SCDL and Ground Truth.

In Fig. 11, we provide the comparison with the state-of-the-art algorithms when applied to the real data scenario. As the testing data cube, we utilize a multispectral scene captured by Landsat-8 on September 17, 2017. Visual observation in both the full-spatial resolution image and the cropped red-square region reveals that the RWL1-SF algorithm produces noisy reconstructions with severe artifacts. Although the K-SVD produces more faithful approximations of the ground truth spectral information, the proposed SCDL algorithm synthesizes spectral observations of a higher quality without introducing noise effects. Quantitatively, the proposed SCDL scheme outperforms other techniques in terms of the evaluation metrics, achieving a PSNR value of 39.75 dB, in contrast to the RWL1-SF and the K-SVD that achieve 23.50 and 33.57 dB, respectively. Similarly, in terms of the SAM error metric, the proposed technique achieves the smallest value of 0.014 as compared to RWL1-SF and K-SVD that achieve 0.224 and 0.032, respectively.

Moreover, in Fig. 12, we depict the difference between the reconstruction by each algorithm and the actual 12th spectral band. As we may observe, both RWL1-SF [Fig. 12(b)] and K-SVD [Fig. 12c)] achieve reconstructions that are noticeably different from the ground truth. In contrast, the difference image attained by our SCDL technique, as depicted in Fig. 12(d), demonstrates a high-quality recovery that matches accurately with the ground truth 12th spectral

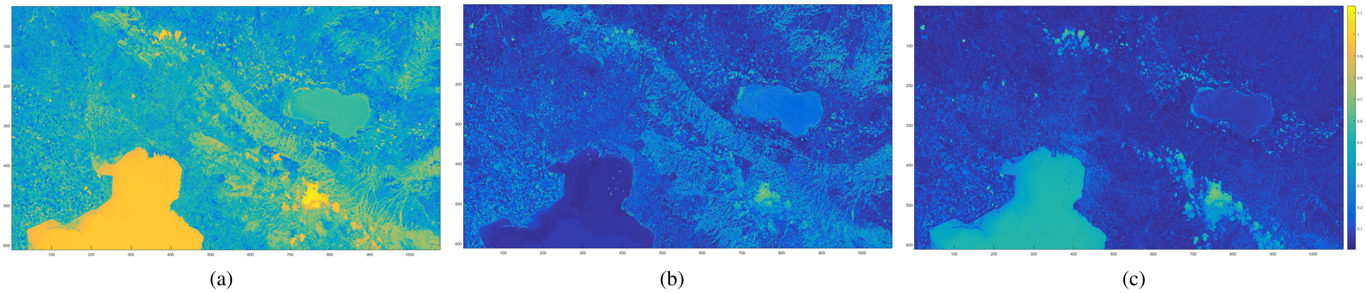

Fig. 13. Real Data Scenario (North Greece Region). In this simulation, we illustrate the Spectral Angle Mapper (SAM) images for the comparable techniques. As we may observe, both the RWLW-SF and the K-SVD algorithms provide more degraded reconstructions, in comparison with the proposed algorithm. In addition, quantitatively, in terms of the error metric, the proposed algorithm achieves a lower SAM value, compared to the other two state-of-the-art approaches. (a) RWSF, SAM: 0.224. (b) SSR-K-SVD, SAM: 0.032. (c) SCDL, SAM: 0.014.

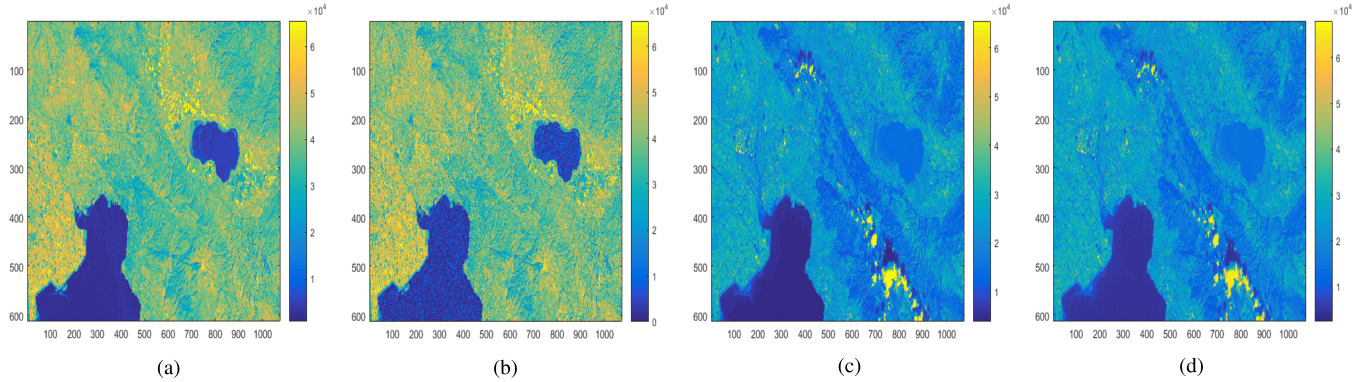

Fig. 14. Hyperspectral Image Denoising. In this experiment, we provide the ground 5th spectral band of the Landsat-8, influenced by the existence of zero mean, and $\sigma^2 = 0.05$ Gaussian noise. (Left to Right) We illustrate the accurate Landsat's-8 5th spectral band, the corresponding noisy observation, the ground truth Sentinel's-2 5th spectral band, and the proposed system's reconstruction. Both in term of visual perception and quantitatively, the proposed scheme achieves a faithful reconstruction of the high-resolution data cube even on the extreme scenario when the input low-spectral resolution part is degraded by noise. (a) Ground truth 5th Landsat's-8 band. (b) Noisy 5th Landsat's-8 band. (c) Ground Truth 5th Sentinel's-2 band. (d) Recovered 5th Sentinel's-2 band.

band. Finally, Fig. 13 demonstrates the SAM images of the compared techniques for the North Greece Region hypercube. We observe that both visually and in terms of the SAM index, the proposed ADMM coupled dictionary learning scheme, outperforms the state-of-the-art approaches. In terms of visual perception, we may notice that our approach provides a high-quality SAM image of the testing hypercube, without introducing noise artifacts. In constrast, both the K-SVD and RWL1-SF techniques, provide lower quality SAM images.

1) Impact on Hyperspectral Image Denoising: In this paragraph, we examine the performance of the proposed SDCL scheme on the fundamental problem of hyperspectral image denoising. In further detail, we considered the real data acquisition scenario, enhancing the spectral dimensions of Landsat-8 to the spectral resolution of the Sentinel-2 sensor. The major difference with the previous paragraphs is that we have also considered the noise existence. Specifically, we assumed that the noise distribution of the low-spectral resolution part adheres to a normal distribution, $N \sim (0, 0.05)$. Consequently, we have added zero-mean ($\mu = 0$) Gaussian noise, with 0.05 standard deviation ($\sigma^2 = 0.05$), to Landsat-8's training examples. The main objective is to recover the 13 spectral bands of the Sentinel-2 sensor using as input the 9 noisy spectral observations of the Landsat-8 instrument. In order to achieve this goal, we have prepared one pair of dictionaries that represent the low resolution and noisy part, and the corresponding high-resolution observations.

Fig. 14 stands as an example of the proposed SCDL scheme applied on the hyperspectral image denoising problem. Specifically, we illustrate the ground truth and the noisy fifth observation of Landsat-8 sensor, along with the synthesized fifth spectral band of Sentinel-2. As we may notice, the proposed coupled dictionary learning algorithm is able to provide a high-quality and spectrally superresolved data cube, from the noisy low-spatial and spectral resolution input.

In addition, in Fig. 15, we depict the comparison with the state-of-the-art algorithms applied to the scenario where the low-spectral resolution part is influenced by the presence of Gaussian noise. Specifically, we illustrate the 12th band of the multispectral testing scene that was utilized in the previous examples (i.e., Figs. 10 and 11). As we may notice, the proposed SCDL scheme outperforms both the K-SVD dictionary learning and the RWL1-SF approaches, both visually but also in terms of quantitative metrics. For instance, the RWL1-SF approach achieves a SAM value of 0.398, the K-SVD reconstruction reaches the SAM value of 0.091, while the proposed SCDL algorithm achieves the smallest of 0.030. Although initial simulation results indicate that the proposed SCDL scheme is also capable of addressing the hyperspectral denoising problem, a detailed analysis of

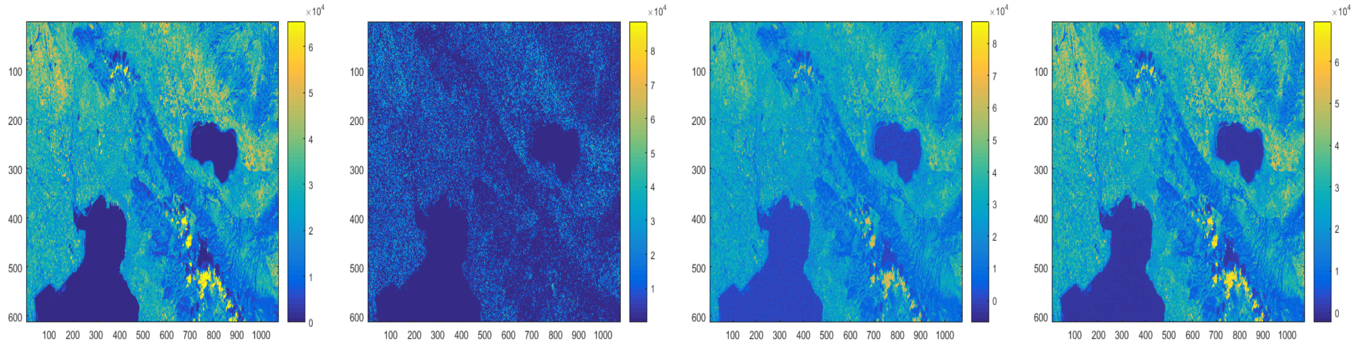

(a) (b) (c) (d)

Fig. 15. Impact of Hyperspectral Image Denoising (Real Data Acquisition—North Greece Region). In this simulation, we examine the reconstruction quality of the comparable techniques when the low-resolution part of the Landsat-8 sensor is degraded by Gaussian noise. For this purpose, we trained coupled dictionaries using Sentinel-2 and noisy Landsat-8 data, scanned in the same spatial locations. To verify our recovery, the output, high-spectral resolution, and denoised hypercube is compared with the ground truth Sentinel-2 data cube. We note that the proposed SCDL scheme outperforms the comparable literature approaches both in visual perception and quantitatively. Consequently, given the appropriate training, the proposed algorithm is able to confront the challenging problem of hyperspectral image denoising. (a) 12th Sentinel's-2 band. (b) RWL1-SF, SAM: 0.398. (c) K-SVD, SAM: 0.091. (d) SCDL, SAM: 0.030.

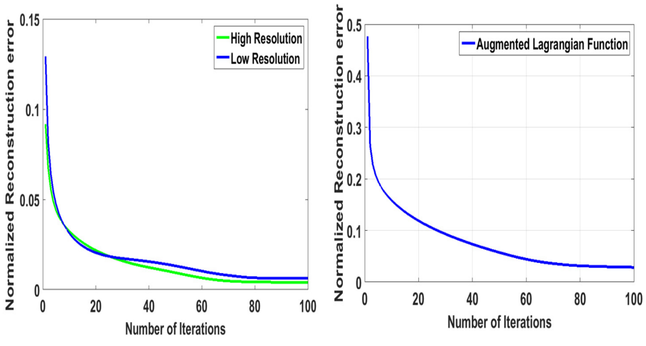

(a) (b)

Fig. 16. Convergence Behavior of the proposed Dictionary Learning Algorithm. (Left) Convergence of the two dictionaries. (Right) Convergence of the augmented Lagrangian function. In all cases, the proposed algorithm converges into a stationary point. (a) Convergence of $\mathbf{D}_h$ and $\mathbf{D}_\ell$. (b) Convergence of the Augmented Lagrangian $\mathcal{L}$.

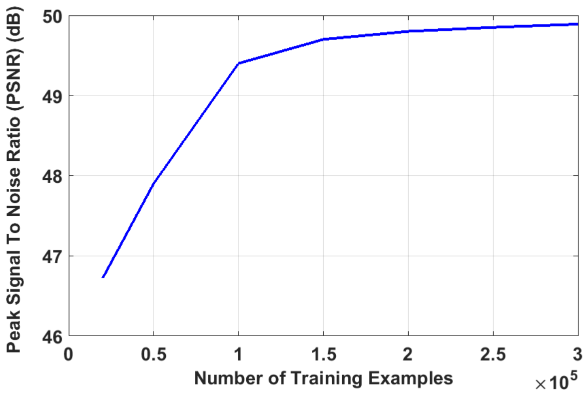

Fig. 17. Cube 5 hyperspectral scene. Sentinel to Hyperion spectral superresolution scenario. In this simulation, we illustrate the PSNR of the proposed SCDL algorithm as a function of the number of training examples. We observe that after approximately 10^5 training examples, SCDL reaches a stable plateau.

the denoising perspectives, including consideration of different types of degradation, and subsequent comparison with state-of-the-art denoising techniques is beyond the scope of this paper, and thus it is left as future work.

C. Convergence

In this section, we investigate the empirical convergence of the proposed algorithm when it is applied on the MODIS to Hyperion spectral superresolution case. Specifically, we examine the convergence behavior of both the high- and low-spectral resolution dictionaries, $\mathbf{D}_h, \mathbf{D}_\ell$, as well as the convergence of the augmented Lagrangian function $\mathcal{L}$. Fig. 16 depicts the normalized reconstruction errors for the two dictionaries and the augmented Lagrangian function as a function of the number of iterations. We note that both dictionaries converge after approximately 20 iterations while the augmented Lagrangian function needs around 60 iterations for convergence. We observed a similar convergence behavior for both the Sentinel-2 to Hyperion and the Landsat-8 to Sentinel-2 spectral superresolution scenarios.

D. Sensitivity to Parameters

In the following paragraphs, we investigate the impact of the parameters selection in our algorithm's performance. First, we examine the number of training examples for the coupled dictionary learning procedure versus the reconstruction quality. Then, we investigate the impact of the dictionary size (number of dictionary atoms) on the reconstruction quality. Finally, we investigate the proper selection of the sparsity regularization parameter (λ) to both the execution time of our algorithm and the reconstruction quality, in terms of PSNR.

To study the sensitivity of the proposed algorithm, we evaluated the reconstruction performance of the coupled trained dictionaries as a function of the number of training examples. In Fig. 17, we provide the PSNR values for the reconstruction of Cube 5 (EO1H1120822017023110K7) hyperspectral scene, as a function of the number of training examples. In this simulation, we use Sentinel's spectral profiles, and thus, we synthesize the full spectrum from 7 spectral observations. Specifically, we investigated the performance of the proposed

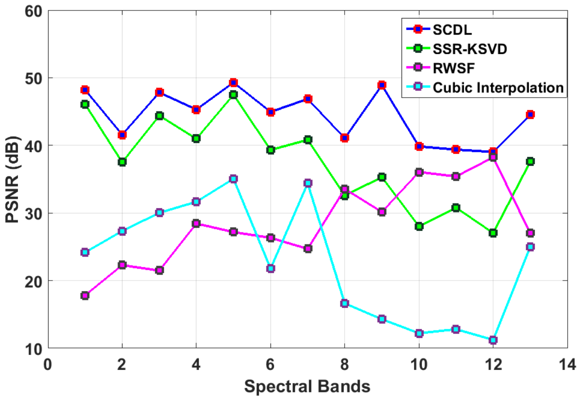

Fig. 18. Landsat-8 to Sentinel-2, real data scenario. Evaluation of the reconstruction quality in terms of the PSNR metric for 14 spectral band indexes. The proposed SCDL scheme achieves consistently higher PSNR values, compared with state-of-the-art approaches.

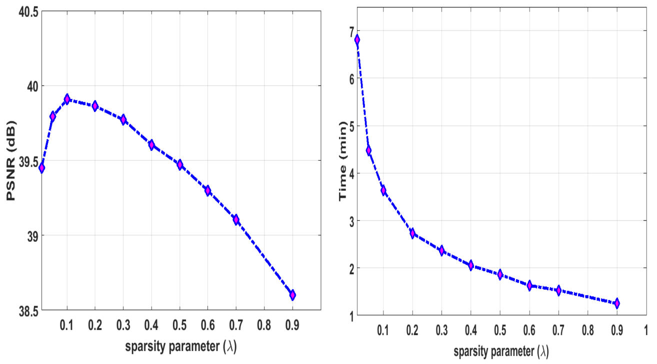

(a) (b)

Fig. 19. (Left to Right) In this experiment, we demonstrate the impact of the sparsity regularization parameter (λ) on the reconstruction performance and on the execution time. As the value of λ increases, the execution time decreases and the reconstruction quality drops. For $\lambda = 0.2$, our system achieves the optimal performance, balancing between a high-quality reconstruction, and a short execution time. (a) Sparsity parameter versus PSNR. (b) Sparsity parameter versus execution time.

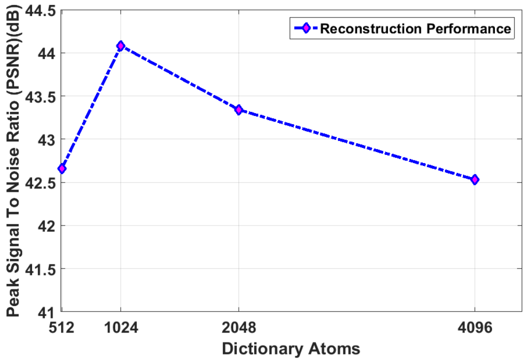

Fig. 20. Reconstruction performance as a function of the dictionary size. In this experiment, we used the hypercube that is depicted in Fig. 5, and we reconstructed the full spectrum composed of 96 spectral bands from only 7 spectral observations. The best performance of 44.04 dB is achieved when we use 1024 dictionary atoms.

scheme when we start from a relatively small size of training examples, i.e., 0.5×10^5, and we gradually increased the training size to 3×10^5 examples. Results indicate that the performance of the SCDL method monotonically increases as a function of the number of input training examples, as expected. However, experimentally we observed that increasing the training size over approximately 1.5×10^5 examples, the PSNR reaches a stationary plateau. We note that after approximately 10^5 training examples, SCDL achieves its highest PSNR value of 49.50 dB. Consequently, for the spectral super-resolution problem, using a larger number than 10^5 training examples in the coupled dictionary learning process offers a marginal improvement to the reconstruction quality. For this reason, we fixed the training size to 10^5 examples.

Fig. 18 demonstrates the PSNR performance for various spectral bands in the Landsat-8 to Sentinel-2 spectral superresolution scenario. Note that for all spectral bands, the proposed SCDL scheme achieves higher reconstruction quality, as compared with the state-of-the-art techniques. On the other hand, Fig. 19 investigates the impact of the sparsity parameter λ, on both the reconstruction quality and the execution time. This experiment was implemented using the Landsat-8 to Sentinel-2 spectral resolution enhancement scenario. Specifically, we used as a test scene, the hypercube that is depicted in Figs. 10 and 11 (North Greece Region). In order to select the proper sparsity regularization parameter for the reconstruction process, we have experimented with several λ values, ranging from 0.1 to 0.9. Specifically, we observed that for $\lambda = 0.1$ our system achieves the highest reconstruction performance in terms of the PSNR error metric. As we gradually increase the value of λ, the execution time decreases dramatically, but unfortunately, the reconstruction quality degrades. The highest PSNR value is achieved for $\lambda = 0.1$. For this value of λ, the proposed scheme reconstructs the high-spectral resolution North Greece hypercube of spatial dimensions (612×1076) in about 2.8 min when the sparse-based RWSF-L1 approach requires approximately 3.2 h. Consequently, the proposed SCDL scheme outperforms the state of the art both in terms of reconstruction performance and execution time. As a result, the optimal selection of the sparsity parameter is crucial for every sparse-based algorithm. We note that in order to achieve a fair comparison with the other two sparse-based algorithms (KSVD and RWSF-L1), we used the same sparse regularization term.

Finally, in Fig. 20, we demonstrate the impact of the dictionary size on the reconstruction performance. In this experiment, we utilized the hypercube that is depicted in Fig. 5, and thus, we reconstructed the full spectrum composed of 96 spectral bands from only 7 spectral observations. Specifically, for a fixed sparsity regularization parameter, $\lambda = 0.2$, we have investigated the impact of using different dictionary sizes consisting of 512, 1024, 2048, and 4096 atoms. It is important to note that as we increase the number of dictionary atoms (> 1024), the reconstruction quality decreases. However, in these cases as well, the proposed recovery outperforms the state of the art. The results indicate that the optimal reconstruction performance is achieved when we use 1024 dictionary

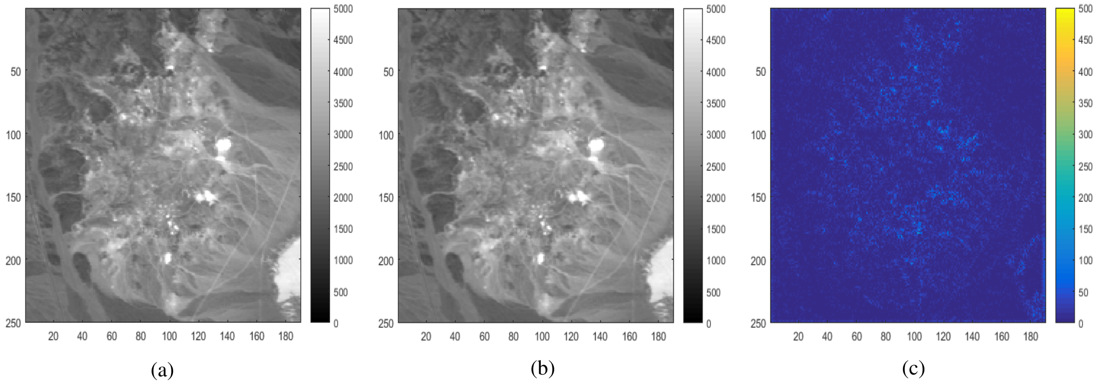

Fig. 21. SCDL recovered 20th AVIRIS Cuprite band, along with the ground truth 20th spectral band, and the absolute difference. We observe that the proposed technique's difference image with respect to the ground truth denotes an accurate reconstruction of the 20th spectral band. (a) Ground Truth 20th Band. (b) SCDL Recovered 20th Band. (c) Difference between SCDL and Ground Truth.

atoms. Similar behavior was observed for all investigated spectral resolution enhancement scenarios.

E. Spectral Coupled Dictionary Learning for Hyperspectral Image Understanding

In the following paragraphs, we examine the impact of the proposed spectral superresolution framework on the fundamental understanding process of hyperspectral unmixing.

Separating a remote sensing image into its elementary components is crucial for multiple applications, including precision agriculture and weather and climate forecasting among others [3]. Consequently, spectral unmixing provides a well-organized mapping of the pure materials that exist in the raw data, by identifying the spectral signatures of these materials (i.e., endmembers) along with their relative contributions (i.e., abundances). The endmembers are assumed to represent the pure materials that are depicted on the hyperspectral scene, while the abundances represent the amount of each endmember that is presented in the pixel.

In order to investigate the hyperspectral unmixing performance after applying the proposed spectral superresolution technique, we exploited a novel linear spectral unmixing algorithm, namely: *fast unmixing algorithm* (FUN) [69]. According to the FUN algorithm, each captured pixel in a hyperspectral scene can be represented as a linear combination between a definite number of endmembers weighted by an abundance factor. The specific technique provides effectively and with low computational complexity simultaneous extraction of the endmembers along with their abundances, by exploiting a modified Gram-Schmidt technique.

Regarding the evaluation setup, we have experimented with the Cuprite scene acquired by the AVIRIS hyperspectral instrument [70]. The specific hyperspectral scene has been widely utilized for both unmixing and classification purposes. In order to demonstrate that the proposed spectral superresolution architecture provides an improvement in the hyperspectral unmixing problem, we adhered to the following experimental scenario: first, we enhanced the spectral dimension of the Cuprite scene using the proposed SCDL scheme, and then, we applied the FUN algorithm for the extraction of the endmembers and abundances. The number of reconstructed endmembers for both the ground truth Cuprite, and the reconstructed from the degraded input, was 12. As a result, we evaluated the unmixing performance in the scenarios when we have the high-spectral versus the low-spectral resolution hypercubes.

In greater detail, the high-resolution data cube was created by removing the noisy (B1-B2 and B221-B224), and water vapor absorption B104-B113 and B148-B167 spectral bands, resulting into 188 spectral observations. For the construction of the low-resolution counterpart, we considered the spectral response functions of the Landsat-8 satellite. In order to provide the correspondence between the two instruments, we constructed the spectral profiles matrix by finding their overlapping wavelength values. Specifically, the overlapping spectral bands among the two instruments are: (B8, B10, B21, B24, B31, B54, B133, B188). The spectral calibration data for the AVIRIS acquisition scenario form a matrix of size 188×8. Consequently, we reconstruct the 188 high-resolution bands of AVIRIS from only 8 spectral observations of Landsat-8 instrument.

Regarding the dictionary training phase, we prepared one pair of dictionaries corresponding to the low (8-bands) and high (188-bands) feature spaces. In addition, we utilized 5 training hypercubes from which 50.000 training hyperpixels were randomly extracted. The number of selected dictionary atoms was set to 512, while the proposed SCDL scheme converged into approximately 30 iterations. Quantitatively, the proposed SCDL scheme reconstructs the Cuprite hyperspectral scene, achieving a PSNR value of 44.41 dB, and a SAM error metric of 0.0368. In Fig. 21, we provide the recovered 20th spectral band of AVIRIS Cuprite scene, using the proposed SCDL scheme, the ground truth 20th spectral and their absolute difference. As we may observe, the proposed SCDL scheme also corresponds with high efficiency in the specific scenario of spectral degradation.

Concluding, in Fig. 22, we evaluate the unmixing performance by comparing the extracted abundancies using the SCDL superresolved hypercubes versus the abundances that were synthesized directly from the low-spectral resolution Cuprite hypercube. As a baseline, we utilize the 12 pub-

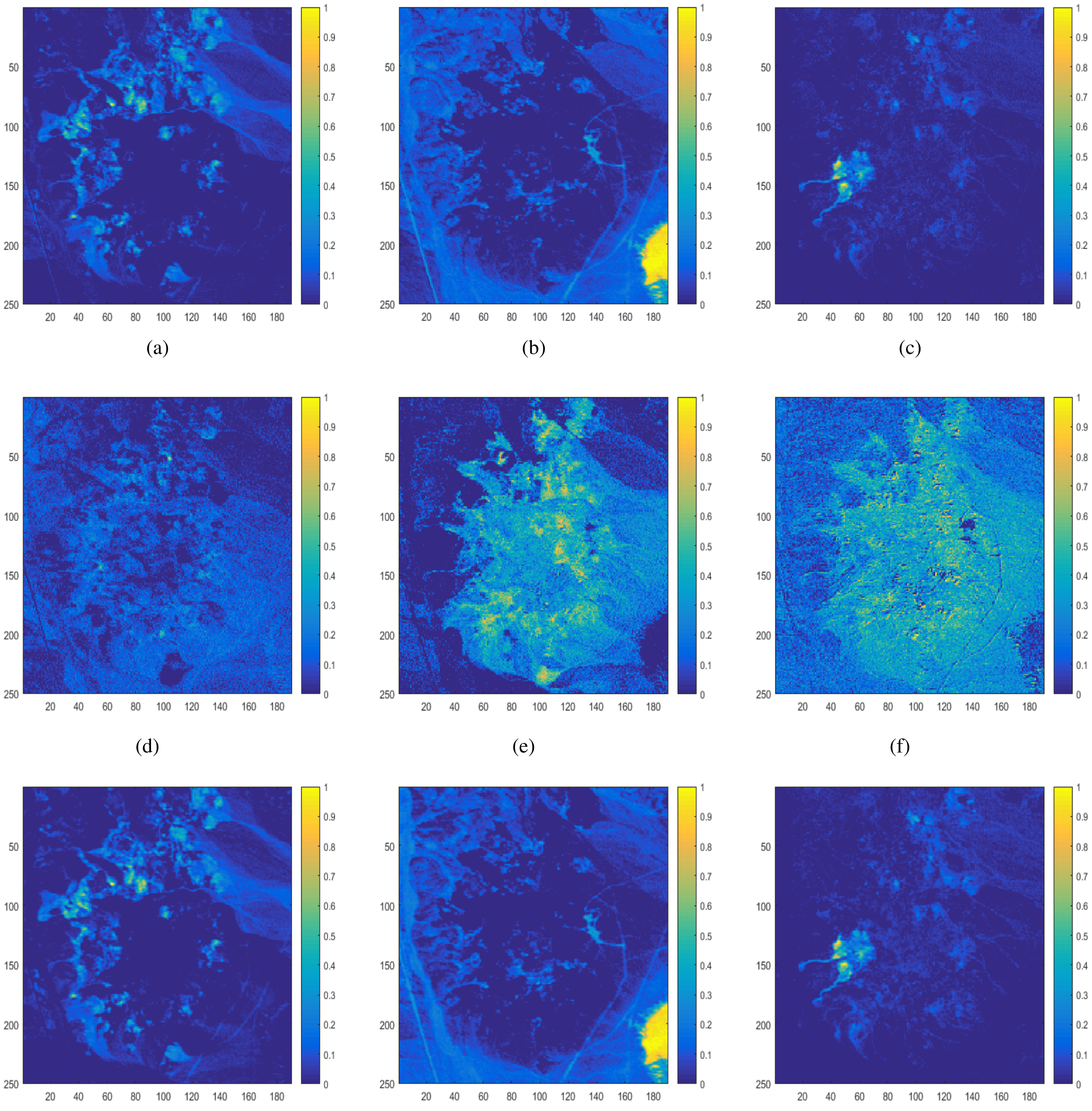

(a) (b) (c)

(d) (e) (f)

(g) (h) (i)

Fig. 22. Unmxing results of the AVIRIS Cuprite hyperspectral scene. Specifically, we illustrate the abundance maps for the extracted #3, #5, and #6 endmembers. (Top to Bottom) In the first row, we depict the ground abundance maps, while in the second row, the unmixing results from the low-resolution Cuprite hypercube are presented. Finally, in the third row, we illustrate the unmixing results from the enhanced Cuprite hypercube. As we may notice, the reconstructed abundances using as input the proposed superresolved hypercube, the present high similarity with the accurate, ground truth abundances. Consequently, the proposed SCDL scheme is able to facilitate the crucial problem of hyperspectral image unmixing. (a) Ground Truth Endmember #3. (b) Ground Truth Endmember #5. (c) Ground Truth Endmember #6. (d) Endmember #3 from Low Resolution. (e) Endmember #5 from Low Resolution. (f) Endmember #6 from Low Resolution. (g) Endmember #3 from SCDL. (h) Endmember #5 from SCDL. (i) Endmember #6 from SCDL.

licly available Cuprite ground truth abundancies [70]. In all cases, we observe that the estimated abundances using the synthesized high-spectral resolution SCDL hypercube provide an accurate reconstruction of the ground truth abundances. Consequently, the proposed SCDL recovery provides a high-quality, superresolved data cube, able to facilitate the hyperspectral unmixing procedure.

VII. CONCLUSION

In this paper, we proposed a novel spectral superresolution architecture for multispectral and hyperspectral imagery, employing the mathematical framework of *sparse representations* through a *coupled dictionary learning* algorithm for encoding the relations between high- and low-spectral resolution scenes. To achieve this goal, an efficient formulation was proposed based on the alternating direction method of multipliers. Experimental results on both synthetic and real remote sensing data support our claim that high-quality reconstruction of multispectral and hyperspectral data is obtained using our method. In addition, the proposed spectral superresolution algorithm is able to provide vital facilitation in subsequent hyperspectral image understanding techniques, such as spectral unmixing and classification. Finally, our scheme can be extended to handle arbitrary low-to-high resolution enhancements by simple modifications of the joint dictionary learning process, and it offers the capability of addressing additional sources of HSI image degradation.

APPENDIX

Derivations of the individual subproblems for the SCDL-ADMM-based dictionary learning scheme, as described in Section IV.

1) *Subproblem* $\mathbf{W}_h$

$$\begin{aligned}\mathbf{W}_h^\star &= \underset{\mathbf{W}_h}{\operatorname{argmin}}\mathcal{L}\\ &\Leftrightarrow \nabla_{\mathbf{W}_h}\left(\frac{1}{2}\|\mathbf{S}_h-\mathbf{D}_h\mathbf{W}_h\|_2^2+\langle Y_1,\mathbf{P}-\mathbf{W}_h\rangle\right.\\ &\qquad+\langle Y_3,\mathbf{W}_h-\mathbf{W}_\ell\rangle\frac{c_1}{2}\|\mathbf{P}-\mathbf{W}_h\|_2^2\\ &\qquad\left.+\frac{c_3}{2}\|\mathbf{W}_h-\mathbf{W}_\ell\|_2^2\right)\\ &= -\mathbf{D}_h^T\cdot(\mathbf{S_h}-\mathbf{D}_h\mathbf{W}_h)-Y_1+Y_3-c_1\\ &\quad\cdot(\mathbf{P}-\mathbf{W}_h)+c_3\cdot(\mathbf{W}_h-\mathbf{W}_\ell).\end{aligned}$$

Setting

$$\begin{aligned}\nabla_{\mathbf{W}_h}\mathcal{L} &= 0\\ &\Leftrightarrow -\mathbf{D}_h\cdot\mathbf{S}_h+\mathbf{D}_h^T\cdot\mathbf{D}_h\cdot\mathbf{W}_h-Y_1+Y_3-c_1\\ &\quad\cdot\mathbf{P}+c_1\cdot\mathbf{W}_h+c_3\cdot\mathbf{W}_h-c_3\cdot\mathbf{W}_\ell=0\\ &\Leftrightarrow \left(\mathbf{D}_h^T\cdot\mathbf{D}_h+c_1\cdot I+c_3\cdot I\right)\cdot\mathbf{W}_h\\ &= \mathbf{D}_h^T\cdot\mathbf{S}_h+Y_1-Y_3+c_1\cdot\mathbf{P}+c_3\cdot\mathbf{W}_\ell\\ &\Leftrightarrow \mathbf{W}_h^\star=\left(\mathbf{D}_h^T\cdot\mathbf{D}_h+c_1\cdot I+c_3\cdot I\right)^{-1}\\ &\quad\times\left(\mathbf{D}_h^T\cdot\mathbf{S}_h+Y_1-Y_3+c_1\cdot\mathbf{P}+c_3\cdot\mathbf{W}_\ell\right).\end{aligned}$$

2) *Subproblem* $\mathbf{W}_\ell$

$$\begin{aligned}\mathbf{W}_\ell &= \underset{\mathbf{W}_\ell}{\operatorname{argmin}}\ \mathcal{L}\\ &\Leftrightarrow \nabla_{\mathbf{W}_l}\left(\frac{1}{2}\cdot\|\mathbf{S}_\ell-\mathbf{D}_\ell\mathbf{W}_\ell\|_2^2+\langle Y_2,\mathbf{Q}-\mathbf{W}_\ell\rangle\right.\\ &\qquad+\langle Y_3,\mathbf{W}_h-\mathbf{W}_\ell\rangle+\frac{c_2}{2}\|\mathbf{Q}-\mathbf{W}_\ell\|_2^2\\ &\qquad\left.+\frac{c_3}{2}\|\mathbf{W}_h-\mathbf{W}_\ell\|_2^2\right)\\ &= -\mathbf{D}_\ell^T\cdot(\mathbf{S}_\ell-\mathbf{D}_\ell\mathbf{W}_\ell)-Y_2\\ &\quad-Y_3-c_2\cdot(\mathbf{Q}-\mathbf{W}_\ell)+c_3\cdot(\mathbf{W}_h-\mathbf{W}_\ell).\end{aligned}$$

Setting

$$\begin{aligned}\nabla_{\mathbf{W}_\ell}\mathcal{L}=0 &\Leftrightarrow -\mathbf{D}_\ell\cdot\mathbf{S}_\ell+\mathbf{D}_\ell^T\cdot\mathbf{D}_\ell\cdot\mathbf{W}_\ell-Y_2-Y_3-c_2\\ &\quad\cdot\mathbf{Q}+c_2\cdot\mathbf{W}_\ell-c_3\cdot\mathbf{W}_h\\ &=0\Leftrightarrow\left(\mathbf{D}_\ell^T\cdot\mathbf{D}_\ell+c_2\cdot I+c_3\cdot I\right)\\ &\quad\cdot\mathbf{W}_\ell=\mathbf{D}_\ell^T\cdot\mathbf{S}_\ell+Y_2+Y_3+c_2\cdot\mathbf{Q}+c_3\\ &\quad\cdot\mathbf{W}_h-c_3\cdot\mathbf{W}_\ell\Leftrightarrow\mathbf{W}_\ell^\star\\ &=\left(\mathbf{D}_\ell^T\cdot\mathbf{D}_\ell+c_2\cdot I+c_3\cdot I\right)^{-1}\\ &\quad\cdot\left(\mathbf{D}_\ell^T\cdot\mathbf{S}_\ell+Y_2+Y_3+c_2\cdot\mathbf{Q}+c_3\cdot\mathbf{W}_h\right).\end{aligned}$$

3) *Subproblem* $\mathbf{P}$

$$\begin{aligned}\mathbf{P}^\star &= \underset{\mathbf{P}}{\operatorname{argmin}}\mathcal{L}\\ &\Leftrightarrow \nabla_{\mathbf{P}}\left(\lambda_h\|\mathbf{P}\|_1+\langle Y_1,\mathbf{P}-\mathbf{W}_h\rangle+\frac{c_1}{2}\|\mathbf{P}-\mathbf{W}_h\|_2^2\right).\end{aligned}$$

a) For $\mathbf{P}>0$

$$\nabla_{\mathbf{P}}\mathcal{L}=\lambda_h\cdot I+c_1\cdot(\mathbf{P}-\mathbf{W}_h)+Y_1$$

. Setting $\nabla_{\mathbf{P}}\mathcal{L}=0$

$$\mathbf{P}^\star=\mathbf{W}_h-\frac{1}{c_1}\cdot(Y_1+\lambda_h\cdot I)$$

b) For $\mathbf{P}<0$

$$\nabla_{\mathbf{P}}\mathcal{L}=-\lambda_h\cdot I+c_1\cdot(\mathbf{P}-\mathbf{W}_h)+Y_1$$

Setting $\nabla_{\mathbf{P}}\mathcal{L}=0$

$$\mathbf{P}^\star=\mathbf{W}_h-\frac{1}{c_1}\cdot(Y_1-\lambda_h\cdot I)$$

Combining

$$\begin{aligned}\mathbf{P}>0\Leftrightarrow\mathbf{W}_h-\frac{1}{c_1}\cdot Y_1>\frac{1}{c_1}\cdot\lambda_h\cdot I\\ \mathbf{P}>0\Leftrightarrow\mathbf{W}_h-\frac{1}{c_1}\cdot Y_1>-\frac{1}{c_1}\cdot\lambda_h\cdot I\end{aligned}$$

we have

$$\left|\mathbf{W}_h-\frac{1}{c_1}\cdot Y_1\right|\le\frac{1}{c_1}\cdot\lambda_h\cdot I.$$

Consequently

$$\mathbf{P}^\star=S_{\lambda_h}\left(\left|\mathbf{W}_h-\frac{Y_1}{c_1}\right|\right)$$

where S_{λ_h} denotes the soft-thresholding operator, defined as

$$S_{\lambda_h}(x)=\operatorname{sign}(x)\cdot\max(|x|-\lambda_h,0).$$

4) *Subproblem* $\mathbf{Q}$

$$\mathbf{Q}^\star=\underset{\mathbf{Q}}{\operatorname{argmin}}\ \mathcal{L}\Leftrightarrow.$$

a) For $\mathbf{Q}>0$

$$\nabla_{\mathbf{Q}}\mathcal{L}=\lambda_\ell\cdot I+Y_2+c_2\cdot(\mathbf{Q}-\mathbf{W}_\ell).$$

Setting $\nabla_{\mathbf{Q}}\mathcal{L}=0$

$$\mathbf{Q}=\mathbf{W}_\ell-\frac{1}{c_2}\cdot(Y_2+\lambda_\ell\cdot I)$$

b) For $\mathbf{Q}<0$

$$\nabla_{\mathbf{Q}}\mathcal{L}=\lambda_\ell\cdot I+Y_2+c_2\cdot(\mathbf{Q}-\mathbf{W}_\ell)$$

Setting $\nabla_{\mathbf{Q}}\mathcal{L}=0$

$$\mathbf{Q}=\mathbf{W}_\ell-\frac{1}{c_2}\cdot(Y_2-\lambda_\ell\cdot I)$$

Combining

$$\begin{aligned}\mathbf{Q}>0\Leftrightarrow\mathbf{W}_\ell-\frac{1}{c_2}\cdot Y_2>\frac{1}{c_2}\cdot\lambda_\ell\cdot I\\ \mathbf{Q}>0\Leftrightarrow\mathbf{W}_\ell-\frac{1}{c_2}\cdot Y_2>-\frac{1}{c_2}\cdot\lambda_\ell\cdot I\end{aligned}$$

we have

$$|\mathbf{W}_\ell - \frac{1}{c_2} \cdot Y_2| \leq \frac{1}{c_2} \cdot \lambda_\ell \cdot I.$$

Consequently,

$$\mathbf{Q}^\star = S_{\lambda_\ell}\left(\left|\mathbf{W}_\ell - \frac{Y_2}{c_2}\right|\right)$$

where S_{λ_ℓ} denotes the soft-thresholding operator, defined as

$$S_{\lambda_\ell}(x) = \text{sign}(x) \cdot \max(|x| - \lambda_\ell, 0).$$

5) *Subproblem* $\mathbf{D}_h$

$$\begin{aligned}\mathbf{D}_h^\star &= \underset{\mathbf{D}_h}{\text{argmin}} \mathcal{L} \\ &\Leftrightarrow \nabla_{\mathbf{D}_h}\mathcal{L} = -(\mathbf{S}_h - \mathbf{D}_h \cdot \mathbf{W}_h) \cdot \mathbf{W}_h^T.\end{aligned}$$

Setting $\nabla_{\mathbf{D}_h}\mathcal{L} = 0$

$$\mathbf{D}_h = \frac{\mathbf{S}_h \cdot \mathbf{W}_h^T}{\phi_h + \delta}$$

where $\phi_h = \mathbf{W}_h \cdot \mathbf{W}_h^T$.

6) *Subproblem* $\mathbf{D}_\ell$

$$\begin{aligned}\mathbf{D}_\ell^\star &= \underset{\mathbf{D}_\ell}{\text{argmin}} \ \mathcal{L} \\ &\Leftrightarrow \nabla_{\mathbf{D}_\ell}\mathcal{L} = -(\mathbf{S}_\ell - \mathbf{D}_\ell \cdot \mathbf{W}_\ell) \cdot \mathbf{W}_\ell^T\end{aligned}$$

Setting $\nabla_{\mathbf{D}_h}\mathcal{L} = 0$

$$\mathbf{D}_\ell = \frac{\mathbf{S}_\ell \cdot \mathbf{W}_\ell^T}{\phi_\ell + \delta}$$

where $\phi_h = \mathbf{W}_\ell \cdot \mathbf{W}_\ell^T$.

REFERENCES

[1] A. Plaza *et al.*, "Recent advances in techniques for hyperspectral image processing," *Remote Sens. Environ.*, vol. 113, pp. S110–S122, Sep. 2009.

[2] J. Jung and M. M. Crawford, "Extraction of features from LIDAR waveform data for characterizing forest structure," *IEEE Geosci. Remote Sens. Lett.*, vol. 9, no. 3, pp. 492–496, May 2012.

[3] J. M. Bioucas-Dias *et al.*, "Hyperspectral unmixing overview: Geometrical, statistical, and sparse regression-based approaches," *IEEE J. Sel. Topics Appl. Earth Observ. Remote Sens.*, vol. 5, no. 2, pp. 354–379, Apr. 2012.

[4] J. Chi and M. M. Crawford, "Spectral unmixing-based crop residue estimation using hyperspectral remote sensing data: A case study at Purdue University," *IEEE J. Sel. Topics Appl. Earth Observ. Remote Sens.*, vol. 7, no. 6, pp. 2531–2539, Jun. 2014.

[5] P. V. Giampouras, K. E. Themelis, A. A. Rontogiannis, and K. D. Koutroumbas, "Simultaneously sparse and low-rank abundance matrix estimation for hyperspectral image unmixing," *IEEE Trans. Geosci. Remote Sens.*, vol. 54, no. 8, pp. 4775–4789, Aug. 2016.

[6] C.-I Chang, *Hyperspectral Imaging: Techniques for Spectral Detection and Classification*, vol. 1. New York, NY, USA: Plenum, 2003.

[7] D. Manolakis and G. S. Shaw, "Detection algorithms for hyperspectral imaging applications," *IEEE Signal Process. Mag.*, vol. 19, no. 1, pp. 29–43, Jan. 2002.

[8] L. Ma, M. M. Crawford, and J. Tian, "Local manifold learning-based-nearest-neighbor for hyperspectral image classification," *IEEE Trans. Geosci. Remote Sens.*, vol. 48, no. 11, pp. 4099–4109, Nov. 2010.

[9] X. Jia, B.-K. Kuo, and M. M. Crawford, "Feature mining for hyperspectral image classification," *Proc. IEEE*, vol. 101, no. 3, pp. 676–697, Mar. 2013.

[10] S. D. Xenaki, K. D. Koutroumbas, A. A. Rontogiannis, and O. A. Sykioti, "A new sparsity-aware feature selection method for hyperspectral image clustering," in *Proc. IEEE Int. Geosci. Remote Sens. Symp. (IGARSS)*, Jul. 2015, pp. 445–448.

[11] *Quickbird*. Accessed: 2001. [Online]. Available: https://www.geoimage.com.au/satellite/quickbird

[12] *Ikonos*. Accessed: 1999. [Online]. Available: https://www.satimagingcorp.com/satellite-sensors/ikonos/

[13] USGS. (2010). *Hyperion*. Accessed: Dec. 7, 2014. [Online]. Available: https://eo1.usgs.gov/sensors/hyperion

[14] *MODIS*. Accessed: 1999. [Online]. Available: https://modis.gsfc.nasa.gov/

[15] *SMAP*. Accessed: 2015. [Online]. Available: https://smap.jpl.nasa.gov/

[16] N. A. Hagen and M. W. Kudenov, "Review of snapshot spectral imaging technologies," *Opt. Eng.*, vol. 52, no. 9, pp. 090901-1–090901-23, Sep. 2013.

[17] G. Tsagkatakis, M. Jayapala, B. Geelen, and P. Tsakalides, "Non-negative matrix completion for the enhancement of snapshot mosaic multispectral imagery," *Electron. Imag.*, vol. 12, no. 12, pp. 1–6, 2016.

[18] G. Tsagkatakis and P. Tsakalides, "Recovery of quantized compressed sensing measurements," *Proc. SPIE*, vol. 9401, p. 940106, Mar. 2015.

[19] *Sentinel-2*. Accessd: 2015. [Online]. Available: https://sentinel.esa.int/web/sentinel/missions/sentinel-2

[20] M. Elad, "Prologue," in *Sparse Redundant Representations*. New York, NY, USA: Springer, 2010, pp. 3–15, doi: doi.org/10.1007/978-1-4419-7011-4.

[21] S. Boyd, N. Parikh, E. Chu, B. Peleato, and J. Eckstein, "Distributed optimization and statistical learning via the alternating direction method of multipliers," *Found. Trends Mach. Learn.*, vol. 3, no. 1, pp. 1–122, Jan. 2011.

[22] Y. Jiao, Q. Jin, X. Lu, and W. Wang. (2016). "Alternating direction method of multipliers for linear inverse problems." [Online]. Available: https://arxiv.org/abs/1601.02773

[23] J. M. Bioucas-Dias, A. Plaza, G. Camps-Valls, P. Scheunders, N. Nasrabadi, and J. Chanussot, "Hyperspectral remote sensing data analysis and future challenges," *IEEE Geosci. Remote Sens. Mag.*, vol. 1, no. 2, pp. 6–36, Jun. 2013.

[24] C. Pohl and J. L. Van Genderen, "Review article multisensor image fusion in remote sensing: Concepts, methods and applications," *Int. J. Remote Sens.*, vol. 19, no. 5, pp. 823–854, 1998.

[25] G. Vivone *et al.*, "A critical comparison among pansharpening algorithms," *IEEE Trans. Geosci. Remote Sens.*, vol. 53, no. 5, pp. 2565–2586, May 2015.

[26] X. X. Zhu and R. Bamler, "A sparse image fusion algorithm with application to pan-sharpening," *IEEE Trans. Geosci. Remote Sens.*, vol. 51, no. 5, pp. 2827–2836, May 2013.

[27] M. T. Eismann and R. C. Hardie, "Hyperspectral resolution enhancement using high-resolution multispectral imagery with arbitrary response functions," *IEEE Trans. Geosci. Remote Sens.*, vol. 43, no. 3, pp. 455–465, Mar. 2005.

[28] X. X. Zhu, C. Grohnfeld, and R. Bamler, "Exploiting joint sparsity for pansharpening: The J-SparseFI algorithm," *IEEE Trans. Geosci. Remote Sens.*, vol. 54, no. 5, pp. 2664–2681, May 2016.

[29] S. Li and B. Yang, "A new pan-sharpening method using a compressed sensing technique," *IEEE Trans. Geosci. Remote Sens.*, vol. 49, no. 2, pp. 738–746, Feb. 2011.

[30] M. Selva, B. Aiazzi, F. Butera, L. Chiarantini, and S. Baronti, "Hyper-sharpening: A first approach on SIM-GA data," *IEEE J. Sel. Topics Appl. Earth Observ. Remote Sens.*, vol. 8, no. 6, pp. 3008–3024, Jun. 2015.

[31] N. Yokoya, T. Yairi, and A. Iwasaki, "Coupled nonnegative matrix factorization unmixing for hyperspectral and multispectral data fusion," *IEEE Trans. Geosci. Remote Sens.*, vol. 50, no. 2, pp. 528–537, Feb. 2012.

[32] Q. Wei, J. Bioucas-Dias, N. Dobigeon, J.-Y. Tourneret, "Hyperspectral and multispectral image fusion based on a sparse representation," *IEEE Trans. Geosci. Remote Sens.*, vol. 53, no. 7, pp. 3658–3668, Jul. 2015.

[33] N. Yokoya, C. Grohnfeldt, and J. Chanussot, "Hyperspectral and multispectral data fusion: A comparative review of the recent literature," *IEEE Geosci. Remote Sens. Mag.*, vol. 5, no. 2, pp. 29–56, Jun. 2017.

[34] C. Jiang, H. Zhang, H. Shen, and L. Zhang, "Two-Step sparse coding for the pan-sharpening of remote sensing images," *IEEE J. Sel. Topics Appl. Earth Observ. Remote Sens.*, vol. 7, no. 5, pp. 1792–1805, May 2014.

[35] H. Shen, X. Meng, and L. Zhang, "An integrated framework for the spatio–temporal–spectral fusion of remote sensing images," *IEEE Trans. Geosci. Remote Sens.*, vol. 54, no. 12, pp. 7135–7148, Dec. 2016.

[36] K. Zhang, M. Wang, and S. Yang, "Multispectral and hyperspectral image fusion based on group spectral embedding and low-rank factorization," *IEEE Trans. Geosci. Remote Sens.*, vol. 55, no. 3, pp. 1363–1371, Mar. 2017.

[37] Y. Wei, Q. Yuan, H. Shen, and L. Zhang, "Boosting the accuracy of multispectral image pansharpening by learning a deep residual network," *IEEE Geosci. Remote Sens. Lett.*, vol. 14, no. 10, pp. 1795–1799, Oct. 2017.

[38] X. Kang, S. Li, and J. A. Benediktsson, "Pansharpening with matting model," *IEEE Trans. Geosci. Remote Sens.*, vol. 52, no. 8, pp. 5088–5099, Aug. 2014.

[39] X. He, L. Condat, J. M. Bioucas-Dias, J. Chanussot, and J. Xia, "A new pansharpening method based on spatial and spectral sparsity priors," *IEEE Trans. Image Process.*, vol. 23, no. 9, pp. 4160–4174, Sep. 2014.

[40] M. Guo, H. Zhang, J. Li, L. Zhang, and H. Shen, "An online coupled dictionary learning approach for remote sensing image fusion," *IEEE J. Sel. Topics Appl. Earth Observ. Remote Sens.*, vol. 7, no. 4, pp. 1284–1294, Apr. 2014.

[41] S. Galliani, C. Lanaras, D. Marmanis, E. Baltsavias, and K. Schindler. (2017). "Learned spectral super-resolution." [Online]. Available: https://arxiv.org/abs/1703.09470

[42] J. Hu, Y. Li, and W. Xie, "Hyperspectral image super-resolution by spectral difference learning and spatial error correction," *IEEE Geosci. Remote Sens. Lett.*, vol. 14, no. 10, pp. 1825–1829, Oct. 2017.

[43] S. Mei, X. Yuan, J. Ji, Y. Zhang, S. Wan, and Q. Du, "Hyperspectral image spatial super-resolution via 3D full convolutional neural network," *Remote Sens.*, vol. 9, no. 11, p. 1139, 2017.

[44] J. Bieniarz, R. Müller, X. X. Zhu, and P. Reinartz, "Hyperspectral image resolution enhancement based on joint sparsity spectral unmixing," in *Proc. IEEE Geosci. Remote Sens. Symp.*, Jul. 2014, pp. 2645–2648.

[45] Y. Zhao, C. Yi, J. Yang, and J. C.-W. Chan, "Coupled hyperspectral super-resolution and unmixing," in *Proc. IEEE Geosci. Remote Sens. Symp.*, Jul. 2014, pp. 2641–2644.

[46] A. Ertürk, M. K. Güllü, D. Çesmeci, D. Gerçek, and S. Ertürk, "Spatial resolution enhancement of hyperspectral images using unmixing and binary particle swarm optimization," *IEEE Geosci. Remote Sens. Lett.*, vol. 11, no. 12, pp. 2100–2104, Dec. 2014.

[47] W. Dong *et al.*, "Hyperspectral image super-resolution via non-negative structured sparse representation," *IEEE Trans. Image Process.*, vol. 25, no. 5, pp. 2337–2352, May 2016.

[48] N. Akhtar, F. Shafait, and A. Mian, "Bayesian sparse representation for hyperspectral image super resolution," in *Proc. IEEE Conf. Comput. Vis. Pattern Recognit.*, Jun. 2015, pp. 3631–3640.

[49] H. Yin, S. Li, and L. Fang, "Simultaneous image fusion and super-resolution using sparse representation," *Inf. Fusion*, vol. 14, no. 3, pp. 229–240, 2013.

[50] J. Yang, J. Wright, T. S. Huang, and Y. Ma, "Image super-resolution via sparse representation," *IEEE Trans. Image Process.*, vol. 19, no. 11, pp. 2861–2873, Nov. 2010.

[51] J. Yang, Z. Wang, Z. Lin, X. Shu, and T. Huang, "Bilevel sparse coding for coupled feature spaces," in *Proc. IEEE Conf. Comput. Vis. Pattern Recognit. (CVPR)*, Jun. 2012, pp. 2360–2367.

[52] L. He, H. Qi, and R. Zaretzki, "Beta process joint dictionary learning for coupled feature spaces with application to single image super-resolution," in *Proc. IEEE Conf. Comput. Vis. Pattern Recognit.*, Jun. 2013, pp. 345–352.

[53] K. Fotiadou, G. Tsagkatakis, B. Moraes, F. B. Abdalla, and P. Tsakalides, "Denoising galaxy spectra with coupled dictionary learning," in *Proc. 25th Eur. Signal Process. Conf. (EUSIPCO)*, Aug. 2017, pp. 498–502.

[54] A. S. Charles, B. A. Olshausen, and C. J. Rozell, "Learning sparse codes for hyperspectral imagery," *IEEE J. Sel. Topics Signal Process.*, vol. 5, no. 5, pp. 963–978, Sep. 2011.

[55] A. S. Charles and C. J. Rozell, "Spectral superresolution of hyperspectral imagery using reweighted ℓ_1 spatial filtering," *IEEE Geosci. Remote Sens. Lett.*, vol. 11, no. 3, pp. 602–606, Mar. 2014.

[56] A. S. Charles, C. J. Rozell, and N. B. Tufillaro, "Sparsity based spectral super-resolution and applications to ocean water color," in *Proc. IGARSS Tech. Abstract*, 2014, pp. 1–4.

[57] K. Fotiadou, G. Tsagkatakis, and P. Tsakalides, "Multi-source image enhancement via coupled dictionary learning," in *Proc. Signal Process. Adapt. Sparse Struct. Represent. Workshop (SPARS)*, 2017, pp. 1–2.

[58] K. Fotiadou, G. Tsagkatakis, and P. Tsakalides, "Spectral resolution enhancement of hyperspectral images via sparse representations," in *Proc. Comput. Imag., IS&T Int. Symp. Electron. Imag.*, 2016, pp. 1–6.

[59] L. Yuan, J. Sun, L. Quan, and H.-Y. Shum, "Image deblurring with blurred/noisy image pairs," *ACM Trans. Graph*, vol. 26, no. 3, p. 1, Jul. 2007.

[60] K. Fotiadou, G. Tsagkatakis, and P. Tsakalides, "Low light image enhancement via sparse representations," in *Proc. Int. Conf. Image Anal. Recognit.* Springer, 2014, pp. 84–93.

[61] M. Aharon, M. Elad, and A. Bruckstein, "K-SVD: An algorithm for designing overcomplete dictionaries for sparse representation," *IEEE Trans. Signal Process.*, vol. 54, no. 11, pp. 4311–4322, Nov. 2006.

[62] Y. Li, X. Xie, and Z. Yang, "Alternating direction method of multipliers for solving dictionary learning models," *Commun. Math. Statist.*, vol. 3, no. 1, pp. 37–55, 2015.

[63] M. Hong, Z.-Q. Luo, and M. Razaviyayn, "Convergence analysis of alternating direction method of multipliers for a family of nonconvex problems," *SIAM J. Optim.*, vol. 26, no. 1, pp. 337–364, 2016.

[64] *Landsat-8*. Accessed: 2013. [Online]. Available: https://landsat.usgs.gov/landsat-8

[65] A. K. Singh, H. V. Kumar, G. R. Kadambi, J. K. Kishore, J. Shuttleworth, and J. Manikandan, "Quality metrics evaluation of hyperspectral images," in *Proc. Int. Arch. Photogramm., Remote Sens. Spatial Inf. Sci.*, vol. 40, no. 8, pp. 1221–1226, 2014.

[66] R. H. Yuhas, A. F. Goetz, and J. W. Boardman, "Discrimination among semi-arid landscape endmembers using the spectral angle mapper (SAM) algorithm," Tech. Rep., 1992.

[67] O. A. De Carvalho and P. R. Meneses, "Spectral correlation mapper (SCM): An improvement on the spectral angle mapper (SAM)," in *Proc. Summaries 9th JPL Airborne Earth Sci. Workshop, JPL Publication*, vol. 9. Pasadena, CA, USA: JPL Publication, 2000.

[68] J. D. O'Sullivan, P. R. Hoy, and H. N. Rutt, "An extended spectral angle map for hyperspectral and multispectral imaging," in *Proc. CLEO, Laser Sci. Photon. Appl.*, May 2011, Paper CMG2.

[69] R. Guerra, L. Santos, S. López, and R. Sarmiento, "A new fast algorithm for linearly unmixing hyperspectral images," *IEEE Trans. Geosci. Remote Sens.*, vol. 53, no. 12, pp. 6752–6765, Dec. 2015.

[70] *Aviris*. Accessed: 2012. [Online]. Available: https://aviris.jpl.nasa.gov/

Konstantina Fotiadou received the B.Sc. degree in applied mathematics from the Department of Applied Mathematics, University of Crete (UoC), Crete, Greece, and the M.Sc. degree in computer science from the Computer Science Department, UoC, in 2011 and 2014, respectively. She is currently pursuing the Ph.D. degree in computer science from the Department of Computer Science, UoC, under the supervision of Prof. P. Tsakalides.

Since 2012, she has been a Research Assistant with the Signal Processing Laboratory, Institute of Computer Science, Foundation for Research & Technology–Hellas, Heraklion, Greece. She is involved in PHySIS and DEDALE European Projects. Her research interests include machine learning techniques for image processing and computational photography applications, and hyperspectral image enhancement techniques.

Grigorios Tsagkatakis received the Diploma and M.S. degrees in electronics and computer engineering from the Technical University of Crete, Chania, Greece, in 2005 and 2007, respectively, and the Ph.D. degree in imaging science from the Rochester Institute of Technology, Rochester, NY, USA, in 2011.

From 2011 to 2013, he was a Marie Curie Post-Doctoral Fellow with the Institute of Computer Science (ICS), Foundation for Research & Technology–Hellas (FORTH), Heraklion, Greece. He is currently a Research Associate with the Signal Processing Laboratory, FORTH–ICS. He has been involved in various European projects, including H2020 PHySIS and DEDALE, FP7 CS-ORION & HYDROBIONETS, FP6 OPTAG, and industry-funded projects by leading companies including Kodak, Rochester, and Cisco, San Jose, CA, USA. He has coauthored more than 30 peer-reviewed conferences, journals, and book chapters in the areas of signal and image processing, computer vision, and machine learning.

Dr. Tsagkatakis was a recipient of the Best Paper Award in the Western New York Image Processing Workshop in 2010 for his paper—A Framework for Object Class Recognition with No Visual Examples.

Panagiotis Tsakalides received the Diploma degree in electrical engineering from the Aristotle University of Thessaloniki, Thessaloniki, Greece, in 1990, and the Ph.D. degree in electrical engineering from the University of Southern California, Los Angeles, CA, USA, in 1995.

He was involved in transferring research and interacting with the industry and projects related to the Small Business Innovation Research and Technology Transfer programs of the U.S. Government. He was the Project Coordinator or Co-Principal Investigator in eight European Commission projects and nine national projects, totally more than 4.5 million euro in actual funding for the University of Crete, Heraklion, Greece, and Institute of Computer Science (ICS), Foundation for Research & Technology–Hellas (FORTH), Heraklion. From 2010 to 2014, he was a Coordinator of the 1.3 Million euro FP7 MC-IAPP CS-ORION Project, conducting research on compressed sensing for remote imaging in aerial and terrestrial surveillance. He is currently a Coordinator of the 1 Million euro H2020 COMPET Project PHySIS, conducting research on sparse signal processing technologies for hyperspectral systems. He is currently a Professor and the Chairman of the Computer Science Department, University of Crete, and the Head of the Signal Processing Laboratory, FORTH–ICS, Heraklion. He has a strong commitment in inspiring young researchers, having supervised 4 Ph.D. and 16 M.Sc. students and 8 post-doctoral fellows. His research interests include statistical signal processing with emphasis in non-Gaussian estimation and detection theory, sparse representations, and applications in sensor networks, audio, imaging, and multimedia systems. He has coauthored over 150 technical publications in these areas, including 30 journal papers.